9248–9265 *Nucleic Acids Research, 2023, Vol. 51, No. 17* *Published online 17 August 2023*
https://doi.org/10.1093/nar/gkad659

Absence of mitochondrial SLC25A51 enhances PARP1-dependent DNA repair by increasing nuclear NAD+ levels

Anka Güldenpfennig[1,2,†], Ann-Katrin Hopp[1,3,†], Lukas Muskalla[1,4], Patrick Manetsch[1,2], Fabio Raith[5], Lars Hellweg[5], Cyril Dördelmann[4,6], Deena M. Leslie Pedrioli[1], Kai Johnsson[5,7], Giulio Superti-Furga[3,8] and Michael O. Hottiger[1,*]

[1]Department of Molecular Mechanisms of Disease (DMMD), University of Zurich, 8057 Zurich, Switzerland, [2]Life Science Zurich Graduate School, Molecular Life Science Ph.D. Program, University of Zurich, 8057 Zurich, Switzerland, [3]Research Center for Molecular Medicine (CeMM) of the Austrian Academy of Science, 1090 Vienna, Austria, [4]Life Science Zurich Graduate School, Cancer Biology Ph.D. Program, University of Zurich, 8057 Zurich, Switzerland, [5]Department of Chemical Biology, Max Planck Institute for Medical Research, 69120 Heidelberg, Germany, [6]Institute of Molecular Cancer Research (IMCR), University of Zurich, 8057 Zurich, Switzerland, [7]Institute of Chemical Sciences and Engineering, Swiss Federal Institute of Technology (EPFL) Lausanne, 1015 Lausanne, Switzerland and [8]Center for Physiology and Pharmacology, Medical University of Vienna, 1090 Vienna, Austria

Received January 13, 2023; Editorial Decision July 16, 2023; Accepted July 31, 2023

ABSTRACT

Though the effect of the recently identified mitochondrial NAD+ transporter SLC25A51 on glucose metabolism has been described, its contribution to other NAD+-dependent processes throughout the cell such as ADP-ribosylation remains elusive. Here, we report that absence of SLC25A51 leads to increased NAD+ concentration not only in the cytoplasm and but also in the nucleus. The increase is not associated with upregulation of the salvage pathway, implying an accumulation of constitutively synthesized NAD+ in the cytoplasm and nucleus. This results in an increase of PARP1-mediated nuclear ADP-ribosylation, as well as faster repair of DNA lesions induced by different single-strand DNA damaging agents. Lastly, absence of SLC25A51 reduces both MMS/Olaparib induced PARP1 chromatin retention and the sensitivity of different breast cancer cells to PARP1 inhibition. Together these results provide evidence that SLC25A51 might be a novel target to improve PARP1 inhibitor based therapies by changing subcellular NAD+ redistribution.

GRAPHICAL ABSTRACT

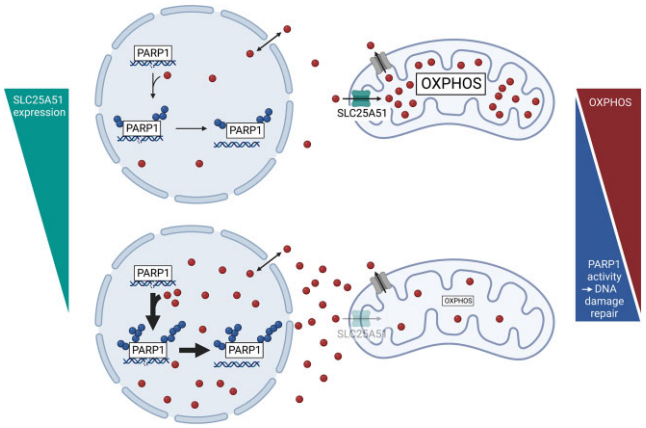

INTRODUCTION

The development of a tight bidirectional relationship between eukaryotic cells and their mitochondria has resulted in a partial spatio-temporal compartmentalization of cell metabolism (1). While certain metabolic enzymes reside solely within mitochondria, others localize to the cytoplasm and/or exist in different isoforms or homologues that are specific to either cellular compartment. Some metabolic reactions are therefore restricted to either the mitochondria or the cytoplasm and others take place in both compartments (2). The synthesis of nicotinamide adenine

*To whom correspondence should be addressed. Tel: +41 44 635 5474; Fax: +41 44 635 5468; Email: michael.hottiger@dmmd.uzh.ch
†The authors wish it to be known that, in their opinion, the first two authors should be regarded as Joint First Authors.

dinucleotide (NAD^+) is an example for a conversion that is believed to be catalyzed in different compartments (3–6).

It was shown that most cultured cells depend on the salvage pathway for NAD^+ synthesis (7). The rate-limiting step is the conversion of nicotinamide (NAM) from the medium to nicotinamide mononucleotide (NMN) catalyzed by nicotinamide phospho-ribosyltransferase (NAMPT). Following this step, nicotinamide mononucleotide adenylyltransferases (NMNATs) catalyze the conversion of NMN to NAD^+. While NAMPT localizes to the nucleus and cytoplasm (8) there are three isoforms of NMNAT. NMNAT1 localizes to the nucleus and NMNAT2 to the cytoplasm. NMNAT3 was reported to be mitochondrial, cytoplasmic and lysosomal, possibly depending on the system (6,9).

The connection of the nuclear and cytoplasmic NAD^+ pools is not yet fully understood. The human nuclear pore complex has an estimated width of 120 nm and is generally expected to allow diffusion of molecules up to at least 30 kDa (10). Thus, small molecules and metabolites, such as NAD^+, are assumed to permeate freely while macromolecules must be transported actively (11). In line with this, similar concentrations of NAD^+ were reported for nucleus and cytoplasm (3,12). NAD^+ diffusion between the nucleus and cytoplasm has recently been shown by transfection of fluorescently-labeled NAD^+, though results from modified NAD^+ might not reflect the biological reality (13). However, the diffusion limit of the nuclear pore complex is known to change in response to different conditions (10). Thus, diffusion of NAD^+ might not be possible in all systems. In line with this, earlier reports suggested that NAD^+ does not diffuse between the nucleus and cytoplasm (14). Further investigation is therefore needed to fully elucidate the regulation of NAD^+ compartmentalization across the cell.

Since NAD^+ is not membrane permeable, the mitochondrial NAD^+ pool was long considered to be fully separate from the other compartments (15). Mitochondrial NADH shuttles were suggested to be the main link to exchange protons between those compartments, thus co-regulating mitochondrial oxidative phosphorylation (OXPHOS) activity and the mitochondrial NAD^+ pool (3–6,15). The recent identification of the solute carrier (SLC) 25A51 as a mitochondrial NAD^+ transporter has however provided strong evidence that, as observed in yeast and plants, a direct exchange of NAD^+ molecules between the cytoplasm and mitochondria is possible and functionally relevant for OXPHOS (16–18). Specifically, lack of SLC25A51 decreases mitochondrial NAD^+, which dampens the cell's oxidative capacity and increases anaerobic glycolysis. Interestingly, the total cellular NAD^+ levels are not affected. Despite its strong effects on both mitochondrial NAD^+ and oxidative metabolism, lack of SLC25A51 only has a mild effect on mitochondrial biogenesis and overall mitochondrial load (17,18). Moreover, SLC25A51 deletion did not induce cell death but strongly reduced proliferation (17,18). Interestingly, comparison of the SLC25A51 expression levels in 341 cell lines revealed that SLC25A51 was co-essential with the expression of proteins involved in electron transport chain function or mitochondrial translation (17).

Since NAD^+ is also an important co-factor for various enzymatic reactions, the observed effects on intracellular NAD^+ pools might affect other intracellular processes beyond OXPHOS and glycolysis. ADP-ribosyltransferases (ARTs) are among the most important cellular NAD^+ consuming enzymes (7). ARTs catalyze ADP-ribosylation by attaching moieties of ADP-ribose from NAD^+ onto either target proteins or nucleic acids (19–21). The activity of ARTs depends on NAD^+ availability (22), tightly linking the modification to metabolism. The nuclear ART PARP1 has a very high affinity to NAD^+ and is known to catalyze extensive nuclear ADP-ribosylation following genotoxic stress to initiate and coordinate the DNA damage response. Based on the synthetic lethality concept, tumors arising in patients who carry germline mutations in either *BRCA1* or *BRCA2* are sensitive to PARP1 inhibition due to the chromatin trapping of PARP1 at unrepaired DNA lesions and subsequent replication-induced DSBs (23,24). Consequently, PARP inhibitors (PARPi) are successfully used in cancer therapy (25–27).

While nuclear ADP-ribosylation has been extensively studied in the last decades, mitochondrial ADP-ribosylation was only recently described in more detail (28,29). Interestingly, nuclear PARP1 activity has been shown to have a strong effect on mitochondrial fitness since PARP1 knockout enhances mitochondrial biogenesis, mitochondrial DNA copy number and OXPHOS rate (30,31). Whether mitochondrial proteins can also directly or indirectly regulate the activity of nuclear PARP1 in a reciprocal manner is not currently known. It is thus intriguing to speculate that controlling subcellular NAD^+ levels via SLC25A51 could also influence ADP-ribosylation and ADP-ribosylation-dependent processes in different subcellular compartments.

MATERIALS AND METHODS

Cell culture

The non-genetically modified cell lines used for this study were originally purchased from ATCC, grown under sterile conditions and routinely tested for mycoplasma. Human U2OS cells, MDA-MB-436 cells and HEK cells stably expressing inducible SLC25A51 were cultured in high glucose containing Dulbecco's Modified Eagle's Medium (DMEM) supplemented with 5% penicillin/streptomycin (P/S) and 10% (v/v) fetal calf serum (FCS). Human U2OS 3xHA-EGFP-OMP25 cells were grown in high glucose containing DMEM supplemented with 5% P/S and 10% (v/v) FCS in the presence of 15 μg/ml blasticidin to maintain selection pressure. Stable U2OS Flp-In™ T-Rex™ cells expressing inducible NAD^+ sensor constructs were cultured in high glucose containing DMEM supplemented with 5% P/S and 10% (v/v) FCS in the presence of 100 μg/ml hygromycin and 15 μg/ml blasticidin and 200 ng/ml doxycycline was added over-night if sensor expression was required. HAP1 WT (Haplogen Genomics) and SLC25A51 knockout cells were grown in Iscove's Modified Dulbecco's Medium (IMDM) supplemented with 10% (v/v) fetal bovine serum (FBS) and 1% P/S.

Table 1. Target sequences for siRNA mediated knockdowns

Name	Sequence
siSLC25A51-1	ATGAGTTCTTGTTAAAGGTTA
siSLC25A51-2	AGGCTCAGATGTCACAGGTTA
siNAMPT	ATGGGTTGCAGTACATTCTTA
siNMNAT1	CAGCCTGATCCTATTGTTGCA
siNMNAT2	CACGGTGATGCGGTATGAAGA
siPARP1	GGUGAUCGGUAGCAACAAA

Table 2. Primer sequences for qPCR

Name	Sequence
RPS12 f	GAAGCTGCCAAAGCCTTAGA
RPS12 r	AACTGCAACCAACCACCTTC
SLC25A51 f	TACCGCAACGACTCACAGTGCT
SLC25A51 r	CCACCAATCTGAGACTGTATGCG
NAMPT f	CCCAAGAGACTGCTGGCATAG
NAMPT r	TCGCTGACCACAGATACAGG
NMNAT1 f	GTGATCTCCGGTAGCACTCG
NMNAT1 r	ACTGTGTACCTTCCTGTTCCA
NMNAT2 f	TGCGGAGTATTGAGGAGTGA
NMNAT2 r	ATCCTGCTGCTGTGTGGTAG
NMNAT3 f	CTATTTCCTGGATGTGCGCA
NMNAT3 r	ATGGGAAGAAAGACCTCGCA
PARP1 f	TCTTTGATGTGGAAAGTATGAAGAA
PARP1 r	GGCATCTTCTGAAGGTCGAT

Drug treatments

Unless otherwise stated, cells were treated with the following compounds at the following concentrations and for the following amount of time: H_2O_2 (50 μM) for 10 or 30 min; methyl methanesulfonate (MMS) (0.013%) for 1h; Olaparib (10 μM) for 24h or as co-treatment with H_2O_2 or MMS; for viability assays, Olaparib and Talazoparib at the indicated concentrations for 6 days; and FK866 (100 μM) for 24h.

siRNA transfection

siRNA mediated knockdowns were performed via reverse transfection using Lipofectamine RNAiMAX (Thermo Fisher) according to the manufacturer's manual. The day after seeding cells into a 6 cm dish, at roughly 40% confluence, 25 nM siRNA were mixed with 5 μl lipofectamine in 500 μl serum-free OptiMEM and incubated for 20 min at room temperature (RT) before being added drop-wise to the cells. 48 h after siRNA transfection, downstream experiments were performed. A scrambled siRNA (siMock) was used as control for each experiment. Sequences for all siRNAs are detailed in Table 1.

Quantitative real-time PCR (qPCR)

RNA isolation and qPCR were performed as previously described (63). In brief, RNA extraction was performed with the NucleoSpin RNA II kit (Macherey-Nagel) and RNA was quantified by NanoDrop. Reverse transcription was performed using the High-Capacity cDNA Reverse Transcription Kit (ThermoFisher/Applied Biosystems) according to the manufacturer's instructions. qPCR was performed using KAPA SYBR® FAST One-Step (Sigma Aldrich) on a Rotor-Gene Q 2plex HRM system (Qiagen). Primer sequences for each gene are detailed in Table 2.

Immunostaining

All IF experiments were performed and quantified as recently described (28). Mitochondria were identified as subobjects associated to each main object (e.g. nucleus) using an intensity-based segmentation based on CoxIV costaining.

For cell cycle analysis, cells were stained with DAPI and imaged as described above (3). The cell cycle profile was plotted based on total and mean DAPI fluorescence intensity and cells were classified into the three cell cycle phases based on the visible peaks. Number of cells in each cell cycle phase was normalized to total cell number (%).

For nuclear pre-extraction, cells were co-treated with PARG inhibitor for the duration of the treatment, and incubated in ice-cold permeabilization solution for 2 min before fixation. When using the eAF1521 macrodomain Fc fusion protein as primary binder, DMEM supplemented with 10% FCS was used for blocking and as dilutant. The following reagents were used for IF at the following concentrations: mouse anti-CoxIV (Abcam, 1:1000), mouse IgG2a-Fc/eAF1521 macrodomain fusion protein (Hottiger laboratory, final concentration 1.64 ng/μl), rabbit anti-CoxIV (Abcam, 1:1000), rabbit pan anti-ADPr antibody (Hottiger laboratory, final concentration 0.4 ng/μl), rabbit anti-ADPr antibody (CST, 1:500), mouse anti-γH2AX (BioLegend, 1:1000), rabbit anti-SLC25A51 (Sigma, 1:100), rabbit anti-PARP1 (CST, 1:500), Alexa Fluor 488 goat-anti-Rabbit IgG (ThermoFisher Scientific, 1:500), Cy3 goat-anti-rabbit IgG (Jackson Immunoresearch, 1:250), Alexa Fluor 488 goat-anti-mouse IgG (Jackson Immunoresearch, 1:250).

Whole cell/tissue lysate preparation, trypsin digestion and ADPr-peptide enrichment

Cells were lysed in lysis buffer (6 M GndHCl, 50 mM Tris pH 8.0), sonicated and then stored at −80°C until LC–MS/MS analysis. Protein disulfide bridges were reduced with 5 mM Tris (2-carboxyethyl)phosphine (TCEP) and alkylated with 10 mM 2-chloroacetamide (CAA) in the dark at 95°C for 10 min.

For whole proteome analyses, 50 μg of proteins were prepared for digestion using the filter aided sample preparation (FASP) methodology (64) and digested with Sequencing Grade Trypsin (1:25; Promega) overnight at 37°C. The samples were then acidified with trifluoroacetic acid (TFA) and salts removed using ZipTip C18 pipette tips (Millipore Corp.). The peptides were eluted with 15 μl of 60% acetonitrile (ACN), 0.1% TFA, dried to completion and then redissolved in 3% ACN, 0.1% formic acid to a final peptide concentration of 0.5 μg/μl.

For ADP-ribosylome analyses, 10 mg of proteins were diluted 1:12 with in PARG buffer (39) and digested with modified Porcine Trypsin (1:25; Sigma) overnight at 37°C. ADPr-Peptide enrichments were carried out as previously described (65) with the following protocol modifications. Following PARG-mediated PAR-to-MAR peptide ADPr-modification reduction, the peptides were enriched using Af1521-WT (0.5 ml beads/15 mg lysate; (39)) and eAF1521

(1.0 ml beads/15 mg lysate; (37)) macrodomain affinity enrichment for 2 h at 4°C. The enriched samples were then prepared for MS analysis as described previously (39).

Liquid chromatography and mass spectrometry analysis

Whole proteome LC–MS/MS analyses were performed either on Orbitrap Fusion Lumos mass spectrometer (Thermo Fisher Scientific), coupled to ACQUITY UPLC liquid chromatographs (Waters). Peptides were loaded onto a commercial MZ Symmetry C18 Trap Column (100 Å, 5 μm, 180 μm × 20 mm, Waters) followed by nanoEase MZ C18 HSS T3 Column (100 Å, 1.8 μm, 75 μm × 250 mm, Waters). Peptides were eluted over 138 min at a flow rate of 300 nl/min. An elution gradient protocol from 2% to 25% B, followed by two steps at 35% B for 5 min and at 95% B for 5 min, respectively, was used. The mass spectrometers were operated in data-dependent mode (DDA) acquiring a full-scan MS spectra (300−1800 m/z) at a resolution of 120 000 at 200 m/z after accumulation to a target value of 500 000. Data-dependent MS/MS were recorded in the linear ion trap using quadrupole isolation with a window of 0.8 Da and HCD fragmentation with 35% fragmentation energy. The ion trap was operated in rapid scan mode with a target value of 10 000 and a maximum injection time of 50 ms. Only precursors with intensities above 5000 were selected for MS/MS and the maximum cycle time was set to 3 s. Charge state screening was enabled. Singly, unassigned and charge states higher than seven were rejected. Precursor masses previously selected for MS/MS measurement were excluded from further selection for 20 s, and the exclusion window was set at 10 ppm. The samples were acquired using internal lock mass calibration on m/z 371.1012 and 445.1200.

Identification of ADP-ribosylated peptides was performed on an Orbitrap Fusion Lumos mass spectrometer (Thermo Fisher Scientific), coupled to ACQUITY UPLC liquid chromatograph (Waters). The ADP-ribose product-dependent method called HCD-PP-EThcD (38) was applied, which includes high-energy data-dependent HCD, followed by high-quality HCD and EThcD MS/MS when two or more ADPr fragment peaks (136.0623, 250.0940, 348.07091 and 428.0372) were observed in the initial HCD scan. A detailed description of the MS parameters can be found in (38). Solvent compositions in channels A and B were 0.1% formic acid in water and 0.1% formic acid in acetonitrile, respectively. Peptides were loaded onto a commercial MZ Symmetry C18 Trap Column (100 Å, 5 μm, 180 μm × 20 mm, Waters) followed by nanoEase MZ C18 HSS T3 Column (100 Å, 1.8 μm, 75 μm × 250 mm, Waters). Peptides were eluted over 110 min at a flow rate of 300 nl/min. An elution gradient protocol from 2% to 25% B, followed by two steps at 35% B for 5 min and at 95% B for 5 min, respectively, was used. All relevant data have been deposited to the ProteomeXchange Consortium via the PRIDE (http://www.ebi.ac.uk/pride) partner repository with the data set identifier PXD031373.

ADP-ribosylome data analysis

MS and MS/MS spectra were converted to Mascot generic format (MGF) using Proteome Discoverer, v2.1 (Thermo Fisher Scientific, Bremen, Germany). The multiple fragmentation techniques HCD and EThcD were utilized, separate MGF files were created from the raw file for each type of fragmentation. Mascot searches were carried out as previously described (38) with the following protocol modifications. The MGFs were searched against the UniProtKB human database (taxonomy 9606, version 20190709), which included 24′905 Swiss-Prot, 34 616 TrEMBL entries, 59 783 decoy hits and 262 common contaminants. Cysteine carbamidomethylation was set as a fixed modification, protein N-terminal acetylation and methionine oxidation were set as variable modifications. Finally, S, R, K, D, E, H, C, T and Y residues were set as variable ADP-ribose acceptor amino acids. The neutral losses of 347.0631 Da and 583.0829 Da from the ADP-ribose were scored in HCD fragment ion spectra (66).

Alkaline comet assays

Cells were treated with 200 μM H_2O_2 for 30 min and left to recover in complete medium for the indicated time points. Following treatment, cells were collected by trypsinization. Harvested cells were embedded in 0.8% SeaPlaque low-melting point agarose (Lonza) on 2-well comet slides (Trevigen) and lysed overnight at 4°C in lysis buffer: 2.5 M NaCl, 100 mM EDTA and 10 mM Tris (pH10), supplemented with 10% DMSO and 1% Triton X-100. For alkaline comet assays, slides were washed after overnight lysis and incubated 40 min in denaturation buffer (300 mM NaOH, 1 mM EDTA) followed by electrophoresis for 20 min at 18 V and 300 mA. Afterward, all slides were washed with PBS, fixed in ice-cold ethanol for 10 min and dried at 37°C. DNA staining was done with SYBR gold (ThermoFisher Scientific) for 10 min, followed by washing with PBS and drying at 37°C. Samples were imaged using the IN Cell Analyzer 2500 HS (GE Healthcare Life Sciences) and analyzed using the Open Comet plugin for Fiji (ImageJ).

Western blotting

For WB analysis, proteins were separated via SDS-page on a 12%-SDS-polyacrylamide gel at 130V. A wet-transfer onto a PVDF membrane was performed at 30 V over-night and membranes were blocked with 5% milk in TBS-T for 1h at RT. Primary antibodies were diluted in 1% milk in TBS-T and incubated at 4°C over night. After three washes, the secondary antibody, diluted in TBS-T, was incubated for 1 h at RT. After another 3 washes, specific proteins/bands were visualized with the Odyssey infrared imaging system (LI-COR).

For SLC25A51 analysis, the membrane was blocked with 10% milk in TBS-T for 2h at RT, followed by a second blocking step in 5% milk in TBS-T for 1 h at RT. The primary antibody was diluted in 5% milk in TBS-T and incubated at 4°C over night. After three washes, the membrane was blocked in 5% milk in TBS-T again for 1 h. The secondary antibody was diluted in 5% milk in TBS-T and incubated for 1h at RT. After another three washes, bands were visualized as described above. The following primary and secondary antibodies were used for WB analysis at the following concentrations: mouse anti-CoxIV (Abcam, 1:1000), rabbit anti-ADPR (CST, 1:1000), IRDye 800 CW goat anti-rabbit IgG

(LI-COR, 1:15000) and IRDye 680RD goat anti-mouse IgG (LI-COR, 1:15000).

Resazurin assay

Cells were seeded to opaque-walled 96-well plates. Following siRNA transfection and/or drug treatment, cell viability and mitochondrial function was assessed by resazurin assay. Cells were washed with PBS and incubated in 100 μl DMEM containing 0.015 mg/ml resazurin sodium salt for 0.5–1.5 h until sufficient fluorescence was reached. Fluorescence was recorded at 560 nm excitation with a 590 nm emission filter. Blank values were subtracted before normalization.

Cell proliferation assay

For Hap1 cells, 100 000 cells were seeded to 24-well plates in duplicates and counted every 24 h for four sequential days using a Countess II FL Automated Cell Counter. For U2OS cells, 50 000 cells were seeded to 24-well plates following reverse siRNA transfection and counted in the same manner.

Measurement of compartmentalized, relative NAD^+ levels using NAD^+-Snifit

Measurements of relative intracellular NAD^+ levels were performed as previously described using the semisynthetic fluorescence biosensor NAD^+-Snifit (32). In short, one day after siRNA transfection or at the same time as plasmid transfection, sensor expression (targeted to either cytoplasm, nucleus or mitochondria) in stable U2OS Flp-In™ cells (18) was induced via administration of 200 ng/ml doxycycline. 12 h later, cells were labeled with 500 nM CP-MaP555-PPT (Supplementary Figure S1B) and 500 nM SiR-Halo for 10–12 h. CP-MaP555-PPT is a derivative of the previously described fluorescent substrate used for labeling of the sensor with better labeling performance and increased sensitivity for NAD^+. After labeling, cells were washed at least three times with DMEM to thoroughly remove any excess of the 2 dyes. Cells were trypsinized and the FRET ratio, as a proxy for NAD^+ levels, was analyzed via flow cytometry using the LRS II Fortessa or BD FACSymphony™. The following laser and filter combination was used: 405 nm to acquire foreword- and sideward scatter, 561 nm (586/15 nm) to acquire the donor signal (CP-MaP555-PPT), 561 nm (635 nm LP, 670/30 nm) to acquire the FRET signal (SiR-Halo) and 640 nm (670/14 nm) to acquire the acceptor (SiR-Halo) only. The data were analyzed using FlowJo. The FRET ratio was calculated by dividing the FRET signal by the donor signal.

Statistical analysis

For statistical analysis of immunofluorescence quantification, the normalized mean fluorescence intensity values of three to five independent experiments were compared. For each experiment, the control mean was arbitrarily set to 30 before log transformation. For NAD^+ measurements and qPCR, the control mean was arbitrarily set to 1. For all experiments with two groups, P values were determined by Student's t-test with $*P < 0.05$; $**P < 0.005$; $***P < 0.0005$. For all experiments with groups of three or more, P values were determined by one-way ANOVA with multiple comparisons analysis. The exact method for multiple comparisons analysis is detailed in the figure legends.

RESULTS

Knockdown of SLC25A51 results in a redistribution of subcellular NAD^+ pools

While lack of SLC25A51 strongly reduced mitochondrial NAD^+ levels, whole cell NAD^+ levels remained unchanged (16–18), pointing towards a redistribution of subcellular NAD^+ to potentially promote cytoplasmic ATP synthesis and other compensatory NAD^+- dependent cellular processes. To analyze subcellular NAD^+ redistribution, we knocked down SLC25A51 and measured subcellular, relative NAD^+ levels using organelle-specific FRET-based NAD^+ sensors (Supplementary Figure S1A (32)) labelled with SiR-Halo (32) and the new, improved substrate CP-MaP555-PPT (Supplementary Figure S1B, unpublished data). To verify sensor functionality, the NAMPT inhibitor FK866 was used as a control for reduction of NAD^+ levels in all compartments (Supplementary Figure S1C–E). Transient knockdown of SLC25A51 in U2OS cells, confirmed by qPCR and immunofluorescence (IF) (Supplementary Figure S1F–H), reduced mitochondrial NAD^+ levels as previously reported (Supplementary Figure S1I, (16–18)). Conversely, NAD^+ accumulated in the cytoplasm following knockdown of SLC25A51, when it can no longer be transported into the mitochondria (Figure 1A). Interestingly, not only cytoplasmic but also nuclear NAD^+ levels were increased after knockdown of SLC25A51 (Figure 1B), pointing towards a direct connection between the NAD^+ pools in these two compartments.

NAMPT knockdown, in addition to SLC25A51 knockdown (Supplementary Figure S1J), reduced NAD^+ levels in both cytoplasm or nucleus to the same extent as in control cells (Figure 1A/B), implying that the increase in cytonuclear NAD^+ is indeed due to a simple redistribution of NAD^+. To further strengthen this conclusion, the expression of important NAD^+ synthesizing enzymes (i.e. *NAMPT, NMNAT1, NMNAT2*) was analyzed by qPCR upon SLC25A51 knockdown. Since the contribution of NMNAT3 to the whole-cell NAD^+ pool is not well understood (17,18,33), the third isoform of NMNAT was excluded from the analysis. Neither the expression of *NAMPT* nor *NMNAT1* and *NMNAT2* significantly changed following SLC25A51 knockdown (Supplementary Figure S1K). Interestingly, immunofluorescence for NAMPT in U2OS cells showed an exclusively nuclear localization (Supplementary Figure S2A), suggesting that in this cell type, NMN is synthesized in the nucleus and may then be converted to NAD^+ in the nucleus but could also diffuse to the cytoplasm via the nuclear pore complex (Supplementary Figure S2B, (34)).

Since nuclear and cytoplasmic NAD^+ both increased after SLC25A51 knockdown, we next assessed if the nuclear and cytoplasmic NAD^+ pools are connected via diffusion of NAD^+ in addition to diffusion of NMN, presumably through the nuclear pore complex. To this end,

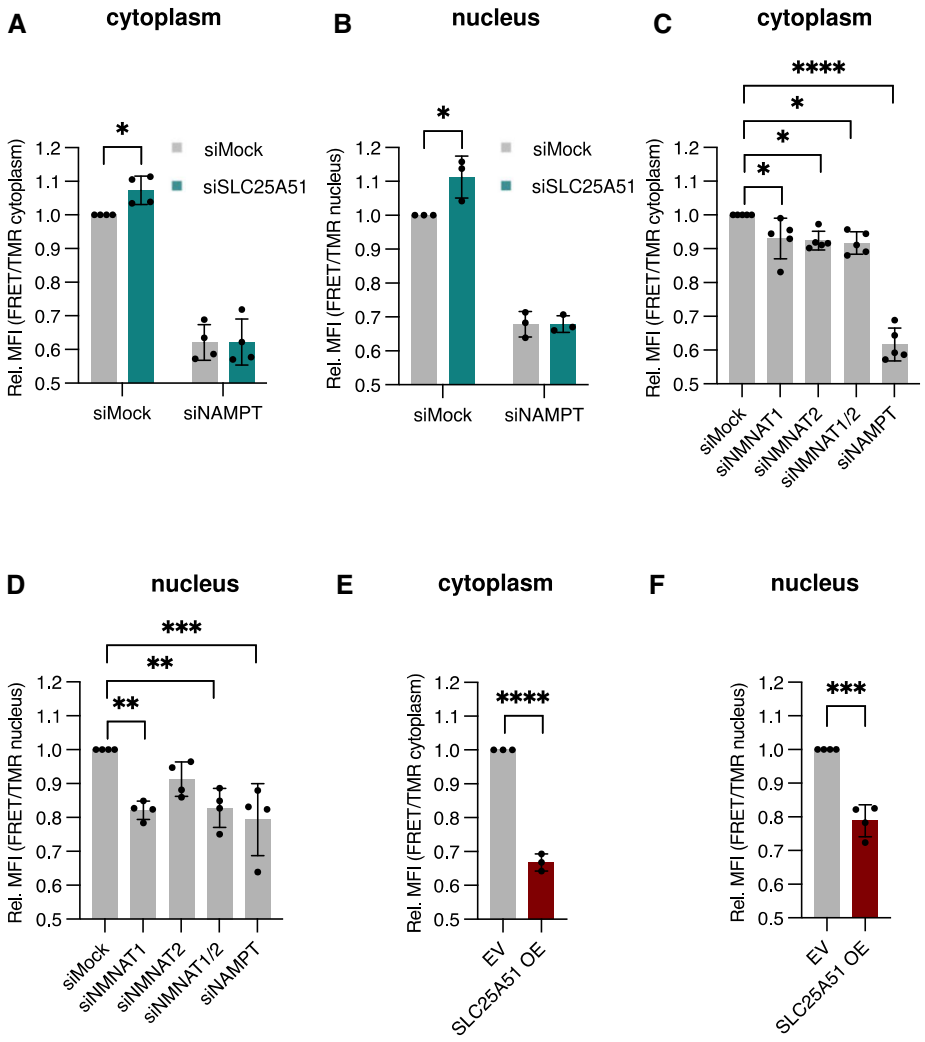

Figure 1. Knockdown of SLC25A51 increases nuclear and cytoplasmic NAD^+ levels without affecting the salvage pathway. (A and B) SLC25A51 was knocked down alone or together with NAMPT in stable U2OS Flp-In™ T-Rex™ cells expressing either an inducible cytoplasmic (**A**) or nuclear (**B**) NAD^+ sensor and NAD^+ levels in the respective compartments were analyzed by flow cytometry 48 h after knockdown. *P* values were determined by one-sample *t*-test for siMock, or unpaired, two-tailed Student's *t*-test for the siNAMPT group. (C and D) NMNAT1 and NMNAT2 were knocked down alone or together, or NAMPT was knocked down in stable U2OS Flp-In™ T-Rex™ cells expressing either an inducible cytoplasmic (**C**) or nuclear (**D**) NAD^+ sensor and NAD^+ levels in the respective compartments were analyzed by flow cytometry 48 h after knockdown. *P* values were determined by one-way ANOVA with multiple comparisons analysis using Dunnett's method. (E and F) HA-tagged SLC25A51 was transiently overexpressed in U2OS Flp-In™ T-Rex™ cells expressing either an inducible cytoplasmic (**E**) or nuclear (**F**) NAD^+ sensor and NAD^+ levels in the respective compartments were analyzed by flow cytometry 24 h after transfection. Cells were co-transfected with GFP and GFP-positive cells were selected to ensure successful overexpression. * $P < 0.05$, ** $P < 0.005$, *** $P < 0.0005$, ns (not significant) not shown.

we knocked down the nuclear NMNAT1 and cytoplasmic NMNAT2, separately or together (Supplementary Figure S2C), and quantified nuclear and cytoplasmic NAD^+ levels. Knockdown of NMNAT1 or NMNAT2 alone as well as both isoforms together reduced NAD^+ levels in both analyzed compartments (Figure 1C, D), implying that both isoforms are required in U2OS cells to maintain the NAD^+ pool in the nucleus and cytoplasm under steady state conditions, and that like NMN, NAD^+ too can diffuse from one compartment to the other. Lastly, to confirm that these effects are directly mediated by the mitochondrial NAD^+ transporter, HA-tagged SLC25A51 was overexpressed in order to assess compartmentalized NAD^+ levels. HA-SLC25A51 overexpression induced a clear HA signal (Supplementary Figure S2D/E) which co-localized with the mitochondrial marker CoxIV (Supplementary Figure S2B), validating overexpression and correct localization of the overexpressed SLC25A51. Overexpression was further confirmed by a strong increase in SLC25A51 expression for cells transfected with HA-SLC25A51 (Supplementary Figure S2F/G). This was previously shown to increase mitochondrial NAD^+ levels (17,18), which was confirmed here (Supplementary Figure S2H). In line with this, overexpression of SLC25A51 severely reduced cytoplasmic as well as nuclear NAD^+ levels (Figure 1E, F). These findings suggest that lack of SLC25A51 does indeed prevent import of NAD^+ synthesized in the cytonuclear compartment into the mitochondria without affecting the import of NAD^+

precursors into the cell, thus resulting in an overall increase of cytoplasmic and nuclear NAD^+ levels. They further underline that SLC25A51 integrates into the classical view of NAD^+ synthesis via the salvage pathway rather than presenting an additional or alternative metabolic route (Supplementary Figure S2B).

Absence of SLC25A51 leads to increased nuclear and reduced mitochondrial ADP-ribosylation

Given the observed increase in cytoplasmic and nuclear NAD^+ levels, it seemed intriguing to investigate if NAD^+-dependent processes, specifically protein ADP-ribosylation, were affected by the absence of SLC25A51. To see if the observed redistribution of NAD^+ would affect intracellular ADP-ribosylation levels, we quantified ADP-ribosylation by IF using a recently developed pan anti-ADP-ribose antibody following both knockdown and knockout (KO) of SLC25A51 in U2OS and Hap1 cells, respectively (28). Organelle-specific co-staining, such as CoxIV and DAPI, were included to define concise masks in which different subcellular ADP-ribosylation signals could be individually measured and quantified as previously described (28,35,36). Similar to the observed changes in NAD^+, knockdown of SLC25A51 resulted in a clear increase in nuclear ADP-ribosylation, while reducing the mitochondrial associated signal (Figure 2A–C). Similarly altered signal intensities were observed when analyzing SLC25A51 KO Hap1 cells (Figure 2D–F). Comparable changes after knockdown or knockout of SLC25A51 were also observed using other ADP-ribosylation specific antibodies and detection tools, including a commercially available pan anti-ADP-ribose antibody (CST) or an engineered macrodomain-Fc fusion protein (37) (Supplementary Figure S3A–E and S3F, G, respectively). Importantly, the signal intensities of the mitochondrial marker CoxIV remained comparable after knockdown or knockout of SLC25A51 (Supplementary Figure S3H/I), confirming that the observed decrease in the mitochondrial signal is unlikely due to a reduction of the overall mitochondrial load.

To confirm that the observed changes in signal intensities were due to a process directly regulated by SLC25A51, we tested whether overexpression of SLC25A51 would increase the mitochondrial signal detected by the anti-ADPR antibody (CST). To this end, we stably integrated doxycycline (DOX)-inducible SLC25A51 in Jump-In HEK cells and quantified mitochondrial ADP-ribosylation signals by IF using the above-described tools after induction with DOX. In agreement with the loss of function results, overexpression of SLC25A51 significantly increased the mitochondrial associated signal detected by CST (Figure 2G, H), suggesting that NAD^+ availability is indeed an important factor for the detected mitochondrial signal intensities. As expected, nuclear ADP-ribosylation remained low when overexpressing SLC25A51 in WT cells (Figure 2G, I).

To investigate whether the observed IF signal intensities associated with different compartments correlate with altered protein ADP-ribosylation, we identified ADP-ribosylated proteins by mass spectrometry-based ADP-ribosylome analyses on WT and SLC25A51 KO Hap1 cells, as previously described (38,39). The overall number of ADP-ribosylated peptide spectral matches (PSM) identified in WT and SCL25A51 KO Hap1 cells was quite similar (Supplementary Figure S3J). Nevertheless, we did note that the overall number of ADP-ribosylated proteins identified in the SLC25A51 KO sample was slightly reduced (Supplementary Figure S3K). Moreover, we found that a fraction of the unique ADP-ribosylated proteins identified in each sample were only modified in either the SLC25A51 KO or WT Hap1 cells (Supplementary Figure S3K and Supplementary Table S1), demonstrating that loss of SLC25A51 and the redistribution in cellular NAD^+ induced shifts in cellular protein ADP-ribosylation, likely dependent on the ADP-ribosyltransferases expressed in the respective compartments. Furthermore, we found that, based on UniProt subcellular localization annotations, the proportion of modified mitochondrial proteins was higher in WT Hap1 cells compared to SLC25A51 KO Hap1 cells (Figure 2J). Indeed, very few mitochondrial ADP-ribosylated proteins were identified in the ADP-ribosylome in SLC25A51 KO cells (Supplementary Figure S3L). In contrast, most proteins that were more strongly ADP-ribosylated in SLC25A51 KO Hap1 cells localized to the nucleus, with a clear increase in total nuclear modified proteins (Figure 2K). Taken together, these data support the conclusion that the redistribution in subcellular NAD^+ induced by loss of SLC25A51 results in altered protein ADP-ribosylation in the analyzed compartments. Furthermore, this highlights that mitochondrial ADP-ribosylation is dependent on NAD^+ import.

Increased nuclear ADP-ribosylation in absence of SLC25A51 is mediated by PARP1

Only three ARTs (PARP1, PARP8 and PARP12) were identified in our mass spectrometry-based ADP-ribosylome of HAP1 cells, with PARP1 being the only writer that was more ADP-ribosylated in SLC25A51 KO cells (Figure 3A). Most of the ADP-ribose acceptor sites with increased modification localize to the auto-modification domain of PARP1 (Supplementary Figure S4A), suggesting that its activity is enhanced in cells lacking SCL25A51. To elucidate the possibility that PARP1 is responsible for the increased nuclear ADP-ribosylation observed previously (Figure 2), we knocked down SLC25A51 alone or together with PARP1 and quantified nuclear ADP-ribosylation by IF. In contrast to the single knockdown of SLC25A51, double knockdown together with PARP1 completely abolished any nuclear ADP-ribosylation signal (Figure 3B, C). Thus, the observed increase in nuclear ADP-ribosylation indeed depends mainly on PARP1 in U2OS cells, while other nuclear ARTs are unlikely to contribute to the observed increased nuclear ADP-ribosylation. This was further strengthend by qPCR data of all ARTs, revealing that PARP1 is by far the most highly expressed ART in U2OS and HAP1 (Supplementary Figure S4B and C). Moreover, Western blotting of Hap1 WT and SLC25A51 KO cells further confirmed that PARP1 is more modified in SLC25A51 KO cells compared to WT cells, since the band corresponding to PARP1

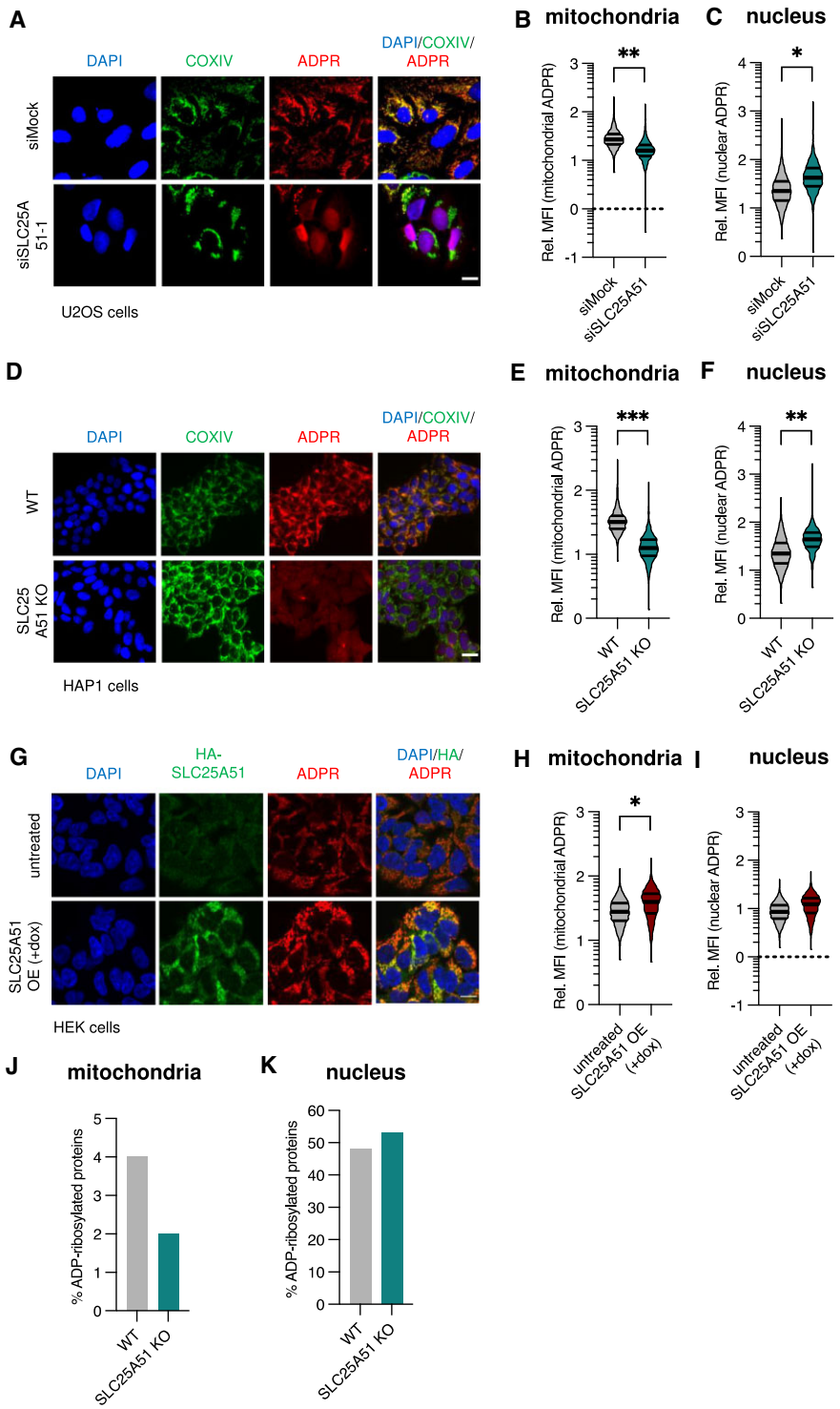

Figure 2. Knockdown or knockout of SLC25A51 decreases mitochondrial and increases nuclear ADP-ribosylation. (A–C) SLC25A51 was knocked down in U2OS cells and ADP-ribosylation was analyzed by IF 48 h after siRNA transfection using a pan anti-ADPR antibody. CoxIV (green) was used as a mitochondrial marker. Representative images are shown on the left (**A**) and mitochondrial (**B**) and nuclear (**C**) quantification on the right. (D–F) ADP-ribosylation was analyzed in HAP1 SLC25A51 knockout cells by IF using a pan anti-ADPR antibody; representative images are shown on the left (**D**) and mitochondrial (**E**) and nuclear (**F**) quantification on the right. (G–I) ADP-ribosylation was analyzed in JumpIn HEK DOX-inducible SLC25A51 wildtype overexpressing cells by IF using a pan anti-ADPR antibody; representative images are shown on the left (**G**) and mitochondrial (**H**) and nuclear (**I**) quantification on the right. IF quantifications show one representative result of at least three independent experiments. *P* values were determined by unpaired, two-tailed Student's *t*-test comparing means from at least three independent experiments. (J and K) ADP-ribosylated peptides in HAP1 SLC25A51 knockout cells were identified using liquid chromatography–tandem mass spectrometry (LC–MS/MS). Number of modified peptides of proteins localized to the mitochondria (**J**) and the nucleus (**K**) are shown. * $P < 0.05$, ** $P < 0.005$, *** $P < 0.0005$, ns (not significant) not shown; scale bars indicate 20 μm.

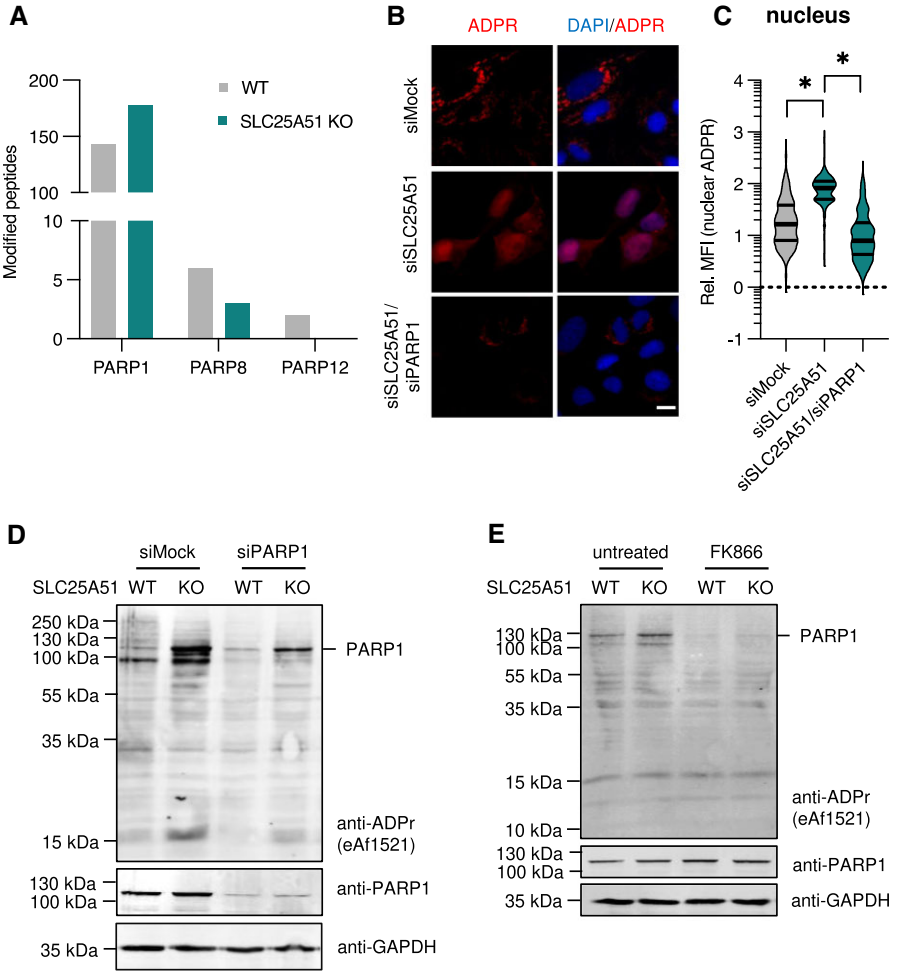

Figure 3. Increased nuclear ADP-ribosylation and DNA damage response in cells lacking SLC25A51 is dependent on PARP1. (**A**) The ADP-ribosylome of HAP1 SLC25A51 knockout cells was identified using LC-MS/MS. Number of modified peptides of different writers of ADP-ribosylation are shown. (B and C) SLC25A51 was knocked down alone and with PARP1, and ADP-ribosylation was analyzed by IF 48 h after siRNA transfection using a pan anti-ADPR antibody; representative images are shown on the left (**B**) and nuclear (**C**) quantification on the right. One representative result of three independent experiments is shown. *P* values were determined by one-way ANOVA with multiple comparisons analysis using Šídák's method, using means from three independent experiments. (**D**) PARP1 was knocked down in Hap1 WT and SLC25A51 KO cells. Cells were lysed 48 h after siRNA transfection and ADP-ribosylation as well as PARP1 expression were analyzed by Western blot. One representative result of three independent experiments is shown. (**E**) Hap1 WT and SLC25A51 KO cells were treated with 1 μM FK866 for 24 h and ADP-ribosylation as well as PARP1 expression were analyzed by western blot. One representative result of three independent experiments is shown. * $P < 0.05$; scale bars indicate 20 μm.

showed stronger modification in SLC25A51 KO cells and was reduced upon PARP1 knockdown (Figure 3D). PARP1 knockdown also reduced ADP-ribosylation of other proteins that were modified in SLC25A51 KO cells (e.g. below 100 or 15 kDa), indicating that not only the automodification of PARP1, but also transmodification of target proteins is affected. Since neither PARP1 expression nor protein abundance was increased in SLC25A51 KO cells (Supplementary Figure S4D, E), the increased nuclear ADP-ribosylation observed in cells lacking SLC25A51 is likely explained by higher substrate availability due to the increased nuclear NAD^+ levels. To test this, Hap1 WT and SLC25A51 KO cells were treated with the NAMPT inhibitor FK866 to reduce overall NAD^+ levels and ADP-ribosylation was assessed by Western blot. FK866 treatment fully reversed the increased ADP-ribosylation observed in cells lacking SLC25A51 (Figure 3E), confirming that the effect is dependent on NAD^+ availability. Taken together, these data highlight that the higher nuclear NAD^+ levels in cells lacking SLC25A51 lead to an enhanced PARP1 activity even under basal conditions.

DNA damage-induced PARP1-mediated ADP-ribosylation is enhanced upon knockdown of SLC25A51

Many of the proteins identified to be stronger ADP-ribosylated in SLC25A51 KO cells by our mass spectrometry-based ADP-ribosylome are known mediators of the DNA damage response (Figure 4A). To assess which cellular processes are associated with the increased nuclear ADP-ribosylation in SLC25A51 KO HAP1 cells, we performed an overrepresentation analysis of all proteins that were at least 5-fold stronger modified in SLC25A51 KO cells compared to Hap1 WT cells

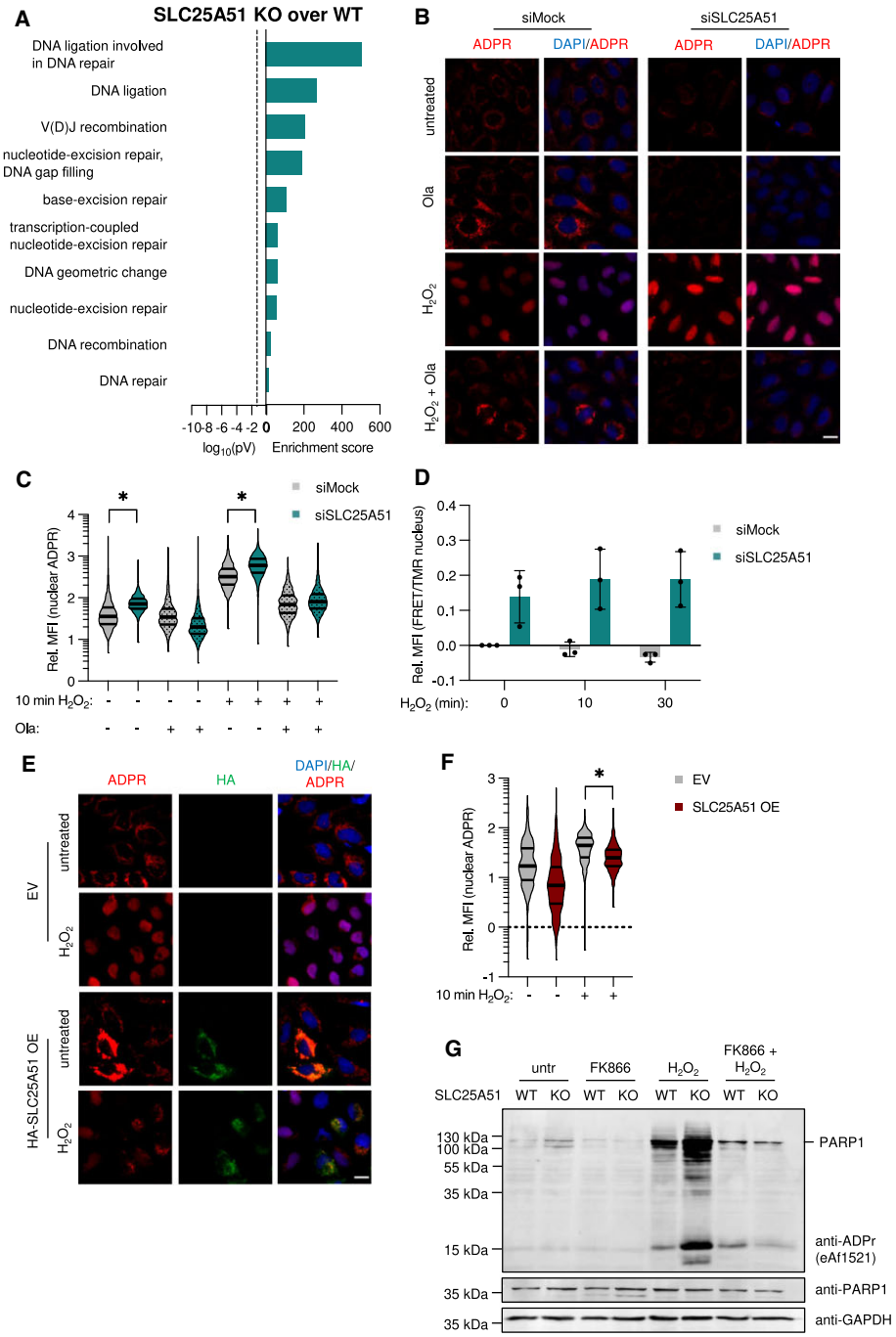

Figure 4. The increase in nuclear ADP-ribosylation in cells lacking SLC25A51 is associated with the DNA damage response. (**A**) ADP-ribosylated peptides in HAP1 SLC25A51 knockout cells were identified using liquid chromatography–tandem mass spectrometry (LC–MS/MS). GO overrepresentation analysis of proteins that were 5-fold more ADP-ribosylated in SLC25A51 KO cells is shown; the enrichment score is displayed to the right and the corresponding *P*-values to the left. (B and C) Following knockdown of SLC25A51, U2OS cells were pre-treated with 10 μM Olaparib for 1 h and treated with 50 μM H_2O_2 in PBS for 10 min (in presence of Olaparib). Nuclear ADP-ribosylation dynamics were monitored by IF (**B**) and quantified (**C**). One representative result of four independent experiments is shown. *P* values were determined by unpaired, two-tailed Student's *t*-test comparing siSLC25A51 to siMock for each time point, using means from four independent experiments. (**D**) Following SLC25A51 knockdown, stable U2OS Flp-In™ T-Rex™ cells expressing an inducible nuclear NAD^+ sensor were treated with 1 mM H_2O_2 in PBS and nuclear NAD^+ levels were measured by flow cytometry after 0, 10 and 30 min. MFI was normalized to untreated siMock cells. *P* values were determined by unpaired, two-tailed Student's *t*-test comparing siSLC25A51 to siMock for each time point, using means from three independent experiments. (E and F) HA-tagged SLC25A51 was transiently overexpressed in U2OS. 24 h after transfection, cells were treated with 50 μM H_2O_2 for 10 min. ADP-ribosylation was analyzed by IF; representative images (**E**) and nuclear quantification (**F**) are shown. One representative result of three independent experiments is shown. *P* values were determined by unpaired, two-tailed Student's *t*-test comparing empty vector (EV) transfected and SLC25A51 overexpression (OE) for each timepoint, using means from five independent experiments. (**G**) Hap1 WT and SLC25A51 KO cells were treated with 1 μM FK866 for 24 h followed by treatment with 50 μM H_2O_2 for 10 min. ADP-ribosylation as well as PARP1 expression were analyzed by western blot. One representative result of three independent experiments is shown. * $P < 0.05$, ns (not significant) not shown; scale bars indicate 20 μm.

(Figure 4A). All identified GO terms were associated with the DNA damage response, implying that the increase in ADP-ribosylation may contribute to DNA damage repair in SLC25A51 KO cells. Interestingly, all processes identified in the overrepresentation analysis of proteins to be more highly modified in Hap1 WT compared to SLC25A51 KO cells, were associated with ribosomes and translation (Supplementary Figure S5A), indicating that compartment-specific processes were regulated. We thus hypothesized that the increase in nuclear ADP-ribosylation following the increased nuclear NAD^+ levels in absence of SLC25A51 might affect the DNA damage response in these cells.

To further investigate this aspect, U2OS cells were treated with 50 μM H_2O_2 for 10 min to induce DNA damage, and cellular ADP-ribosylation was monitored by IF as described above. Knockdown of SLC25A51 significantly increased the amount of nuclear ADP-ribosylation both in untreated cells and following H_2O_2 treatment (Figure 4B and C), suggesting that the absence of NAD^+ transport into the mitochondria allows for a higher induction of nuclear ADP-ribosylation. Nuclear NAD^+ measurements after knockdown of SLC25A51 further confirmed an increase in nuclear NAD^+ availability even after 30 min of H_2O_2 compared to control cells (Figure 4D). Olaparib treatment inhibited the induction of nuclear ADP-ribosylation both in control and SLC25A51 knockdown cells (Figure 4B/C), comparable to PARP1 knockdown (Supplementary Figure S5B/C) which is in agreement with earlier findings (Figure 3B, C). To investigate whether overexpression of SLC25A51 would reduce the H_2O_2 induced ADP-ribosylation, SLC25A51 was overexpressed in U2OS cells and cells again treated with H_2O_2 to induce DNA damage. Consistent with decreased nuclear NAD^+ levels in cells overexpressing the mitochondrial NAD^+ transporter, ADP-ribosylation was significantly lower in SLC25A51 OE cells (Figure 4E, F). Comparably to the results in U2OS cells with transient SLC25A51 knockdown, 10 min H_2O_2 treatment of Hap1 cells induced modest ADP-ribosylation in WT cells, but much stronger ADP-ribosylation in SLC25A51 KO cells when analyzed by Western Blot (Figure 4G) and Immunofluorescence (Supplementary Figure S5D, E). As previously shown in untreated cells, this increase in ADP-ribosylation was dependent on NAD^+ availability since FK866 treatment fully reversed the effect (Figure 4G). Moreover, the observed ADP-ribosylation was again reduced upon knockdown of PARP1 in SLC25A51 KO cells (Supplementary Figure S5F). To confirm that these observations are not an H_2O_2-specific effect, U2OS cells were treated with the alkylation damage-inducing agent methyl methanosulfonate (MMS) and nuclear ADP-ribosylation was monitored by IF. Again, SLC25A51 knockdown significantly increased nuclear ADP-ribosylation following MMS treatment that was reduced by Olaparib (Supplementary Figure S5G/H), suggesting that the increased nuclear NAD^+ levels regulate genotoxic stress responses induced by different compounds. Taken together, these data show that SLC25A51, by regulating nuclear NAD^+ availability, controls nuclear ADP-ribosylation catalyzed by PARP1 independently of the type of genotoxic stress.

H_2O_2-induced phosphorylation of H2AX is reduced and recovery from single-strand breaks improved in absence of SLC25A51

To analyze if the increased PARP1-mediated ADP-ribosylation observed in absence of SLC25A51 contributes to a more efficient DNA damage response, alkaline comet assays were performed to analyze single-strand (SSB) DNA breaks in U2OS cells lacking the transporter. Consistent with an increase in nuclear ADP-ribosylation in SLC25A51 depleted cells even in untreated conditions, SLC25A51 knockdown cells had fewer lesions (Figure 5A and Supplementary Figure S6A), indicating a better baseline repair of damage by constant stressors of endogenous and exogenous origin. Thus, we assessed if SLC25A51 overexpression would have the opposite effect. Upon replication, unrepaired SSBs can lead to the formation of double-strand breaks (DSBs) (40). A critical signal of the DSB response is the phosphorylation of H2AX at Ser139 (γH2AX), which serves as a platform for the recruitment of DNA repair factors at DSBs and can therefore be used as a DSB marker (41–44). Following treatment with SSB inducing agents like H_2O_2 and MMS, a lower γH2AX signal therefore implies a faster SSB response, resulting in a decreased incorporation of SSBs. Strikingly, overexpression of the transporter in U2OS cells was sufficient to induce a clearly detectable γH2AX signal even in absence of a DNA damage stimulus (Figure 5B, C), underlining the importance of nuclear NAD^+ for repair of inherent DNA damage even under basal conditions.

Next, we investigated if SLC25A51 would also affect the DNA damage response following a direct DNA damage stimulus. Following SLC25A51 knockdown, U2OS cells were treated with H_2O_2 and harvested either directly or after recovery in complete medium for 2 or 4 h (Figure 5D and Supplementary Figure S6A, B). While cells lacking SLC25A51, immediately following H_2O_2 treatment, showed a comparable number of lesions to the control, they had significantly fewer lesions after 2 and 4 h of recovery, respectively (Supplementary Figure S6B). To account for a slight trend towards fewer lesions in SLC25A51 knockdown cells even directly following H_2O_2 treatment, lesions after 2 and 4 h recovery were normalized to the first timepoint, H_2O_2 treatment without recovery. Strikingly, SLC25A51 knockdown cells not only had significantly fewer lesions than siMock cells after 2 h but even showed a comparable number of lesions after 2 h of recovery as control cells after 4 h (Figure 5D), suggesting that the repair kinetics are indeed faster in SLC25A51 knockdown cells.

To further analyze the effect of SLC25A51 on the efficiency of the DNA damage response, we investigated whether H_2O_2 induced γH2AX would be affected by SLC25A51 as well. H_2O_2 induced a robust γH2AX signal after 30 min of treatment followed by 2 h of recovery (Figure 5E/F). Knockdown of SLC25A51 significantly reduced the extent of γH2AX (Figure 5E, F). A reduction in γH2AX could either be caused by fewer lesions, indicative of better repair, or impaired signaling, implying reduced repair capacity instead. To assess if the reduction in H_2O_2-induced γH2AX apparent in cells lacking SLC25A51 is dependent on ADP-ribosylation, SLC25A51

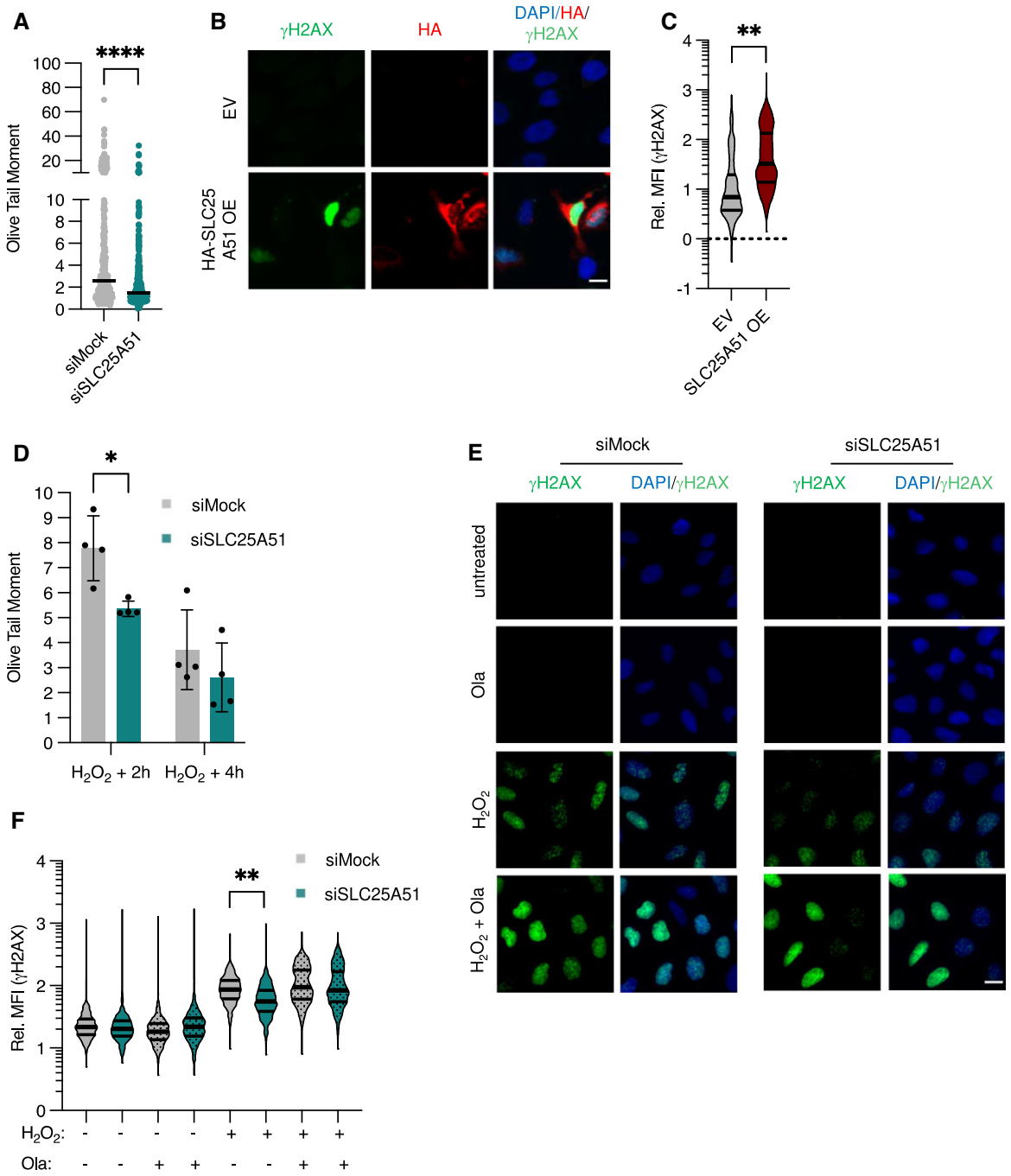

Figure 5. SLC25A51 knock-down improves DNA damage repair. (**A**) SLC25A51 was knocked down in U2OS cells, cells were harvested and analyzed by alkaline comet assay. One representative experiment is shown. *P* values were determined by Kruskal–Wallis test due to non-gaussian distribution of points. (B and C) HA-tagged SLC25A51 was transiently overexpressed in U2OS. 24 h after transfection, cells were treated with 50 μM H_2O_2 for 10 min and subsequently incubated in complete medium for 2 h of recovery. γH2AX was analyzed by IF; representative images (**B**) and quantification (**C**) are shown. One representative result of three independent experiments is shown. P values were determined by unpaired, two-tailed Student's *t*-test, using means from four independent experiments. (**D**) Following knockdown of SLC25A51, U2OS cells were treated with 200 μM H_2O_2 in PBS for 30 min and subsequently incubated in complete medium for 0, 2 or 4 h of recovery. Cells were harvested and analyzed by alkaline comet assay. Olive Tail Moment was normalized to 0 h recovery. Medians of four independent experiments are shown. *P* values were determined by Welch's *t*-test, comparing siSLC25A51 to siMock for each time point. (E and F) Following knockdown of SLC25A51, U2OS cells were pre-treated with 10 μM Olaparib for 1 h and then treated with 200 μM H_2O_2 in PBS for 30 min (in presence of Olaparib) and subsequently incubated in complete medium for 2 h of recovery (in presence of Olaparib). γH2AX formation was analyzed by IF (**E**) and quantified (**F**). One representative result of four independent experiments is shown. *P* values were determined by unpaired, two-tailed Student's *t*-test comparing siSLC25A51 to siMock for each time point, using means from four independent experiments. * $P < 0.05$, ** $P < 0.005$, **** $P < 0.00005$, ns (not significant) not shown; scale bars indicate 20 μm.

knockdown cells were treated with the PARPi Olaparib together with H_2O_2, and γH2AX was analyzed by IF. Olaparib clearly increased H2AX phosphorylation in cells lacking SLC25A51 to levels comparable to the control (Figure 5E, F), indicating that ADP-ribosylation is required for the improved DNA damage response in cells lacking SLC25A51. In line with this, though SLC25A51 knockout or longer-term knockdown reduces proliferation (Supplementary Figure S6C, D), which can also dampen the formation of γH2AX, no effect on proliferation was observed 48 h after knockdown (Supplementary Figure S6D), at which point H2AX phosphorylation was assessed. Furthermore, SLC25A51 KO or knockdown did not induce cell cycle arrest (Supplementary Figure S6E, F). Taken together, these data show that the improved DNA damage response observed in cells lacking SLC25A51 is not purely a proliferation effect but instead depends on ADP-ribosylation, and that the overall repair capacity is not affected by the knockdown of SCL25A51. A similar effect was observed following treatment with MMS as another DNA damage inducing agent. Knockdown of SLC25A51 in U2OS reduced γH2AX after MMS treatment, and Olaparib again reversed this (Supplementary Figure S6G/H). This was further confirmed in Hap1 SLC25A51 KO cells (Supplementary Figure S6I). MMS treatment increased γH2AX levels in WT but not SLC25A51 KO cells (Supplementary Figure S6I), implying that the single-strand damage induced by MMS is repaired faster in Hap1 cells lacking SLC25A51. As previously published, Olaparib treatment alone already induced a strong γH2AX signal (45), underlining a general dependence on PARP1 for ongoing DNA repair, even in absence of a direct genotoxic stress (Supplementary Figure S6I).

Taken together, these results show that SLC25A51 regulates the DNA damage response by limiting PARP1 activity.

PARP1 chromatin retention and sensitivity to PARP inhibitors are reduced in absence of SLC25A51

In presence of a DNA damage stimulus, PARP1 binds to damage sites and automodifies itself. The resulting PAR chains function as a scaffold for the recruitment of repair factors and lead to release of PARP1 from the chromatin once a high enough level of modification is reached (46). In the presence of PARP inhibitors, PARP1 still binds to damage sites but is unable to modify itself, thus remaining tightly bound on the chromatin (Supplementary Figure S7A). PARP1 chromatin retention is therefore inversely correlated to its activity. Since PARP1 activity is increased in cells lacking SLC25A51, we next tested if this would affect PARP1 chromatin retention. Following SLC25A51 knockdown, U2OS cells were co-treated with MMS to induce DNA damage, and Olaparib to induce PARP1 chromatin retention. Cells were analyzed by IF following chromatin pre-extraction. As expected, MMS alone had no effect on PARP1 chromatin retention in either control or SLC25A51 knockdown cells (Figure 6A, B). While treatment of cells with MMS/Olaparib increased the amount of chromatin-bound PARP1, knockdown of SLC25A51 reduced the amount of chromatin-bound PARP1 (Figure 6A, B). These findings indicate that the increased nuclear NAD^+ does indeed compete with Olaparib and thus, allows PARP1 to be released from the chromatin. Increasing the PARPi concentration 5-fold however restored the observed chromatin retention to control levels, confirming that NAD^+ compartmentalization and intracellular availability regulated by SCL25A51 modulate nuclear PARP1 chromatin retention (Figure 6A, B).

PARPi like Olaparib and Talazoparib are used as treatments in different cancer subtypes including breast cancer with BRCA mutations where monotherapy with PARPi has shown promising results in patient cohorts (47–49). Mechanistically, PARPi sensitivity is explained by an increase in PARP1 chromatin retention that leads to DNA SSBs which cannot be repaired in cells where BRCA is missing or mutated (23,24). Due to the reduced PARP1 chromatin retention observed in cells with knockdown of SLC25A51, we hypothesized that SLC25A51 knockdown would also decrease sensitivity of BRCA1-deficient cell lines to PARPi. SLC25A51 was knocked down in Talazoparib-sensitive MDA-MB-436 cells (Supplementary Figure S7B, (50)), followed by treatment with different concentrations of Talazoparib for 6 days. SLC25A51 knockdown clearly increased the IC_{50} of Talazoparib (Figure 6C), which is likely explained by the higher nuclear NAD^+ levels competing with the PARPi. As a control, Talazoparib insensitive U2OS cells were treated with the same range of Talazoparib concentrations for 6 days. Cell viability was reduced by very high Talazoparib concentrations of Talazoparib but not to the same extent as MDA-MB-436 siSLC25A51 cells (Supplementary Figure S7C), showing that SLC25A51 knockdown does not confer complete resistance. To assess if the effect observed in MDA-MB-436 is a cell-specific effect or a general effect of SLC25A51 on PARPi sensitivity, SLC25A51 was knocked down in two other PARPi sensitive cell lines, Olaparib-sensitive MCF7 and MDA-MB-231 (Supplementary Figure S7B). Cells were treated with different concentrations of Olaparib for 6 days. Again, SLC25A51 knockdown reduced Olaparib sensitivity (Supplementary Figure S7D, E), confirming that lack of SLC25A51 affects PARPi sensitivity in a cell type-independent manner. These results suggest that the increased nuclear NAD^+ concentration induces PARP1 activation and subsequently leads to reduced chromatin retention in presence of PARPi, thus partially overcoming the synthetic lethality concept normally observed in BRCA deficient cell lines.

DISCUSSION

SLC25A51 was recently identified as a mitochondrial NAD^+ transporter and its effect on mitochondrial oxidative metabolism was extensively characterized by three independent groups (16–18). However, potential effects on the remaining cellular compartments were not investigated so far. Here, we demonstrate that SLC25A51 knockdown leads to a redistribution of mitochondrial NAD^+ to the nuclear and cytoplasmic compartment and provide evidence that this redistribution has functional consequences beyond affecting glucose metabolism, by increasing PARP1 activity, improving the DNA damage response and reducing PARPi efficacy.

Most cultured cell lines generate NAD^+ predominantly via the salvage pathway and synthesis of NAD^+ from its

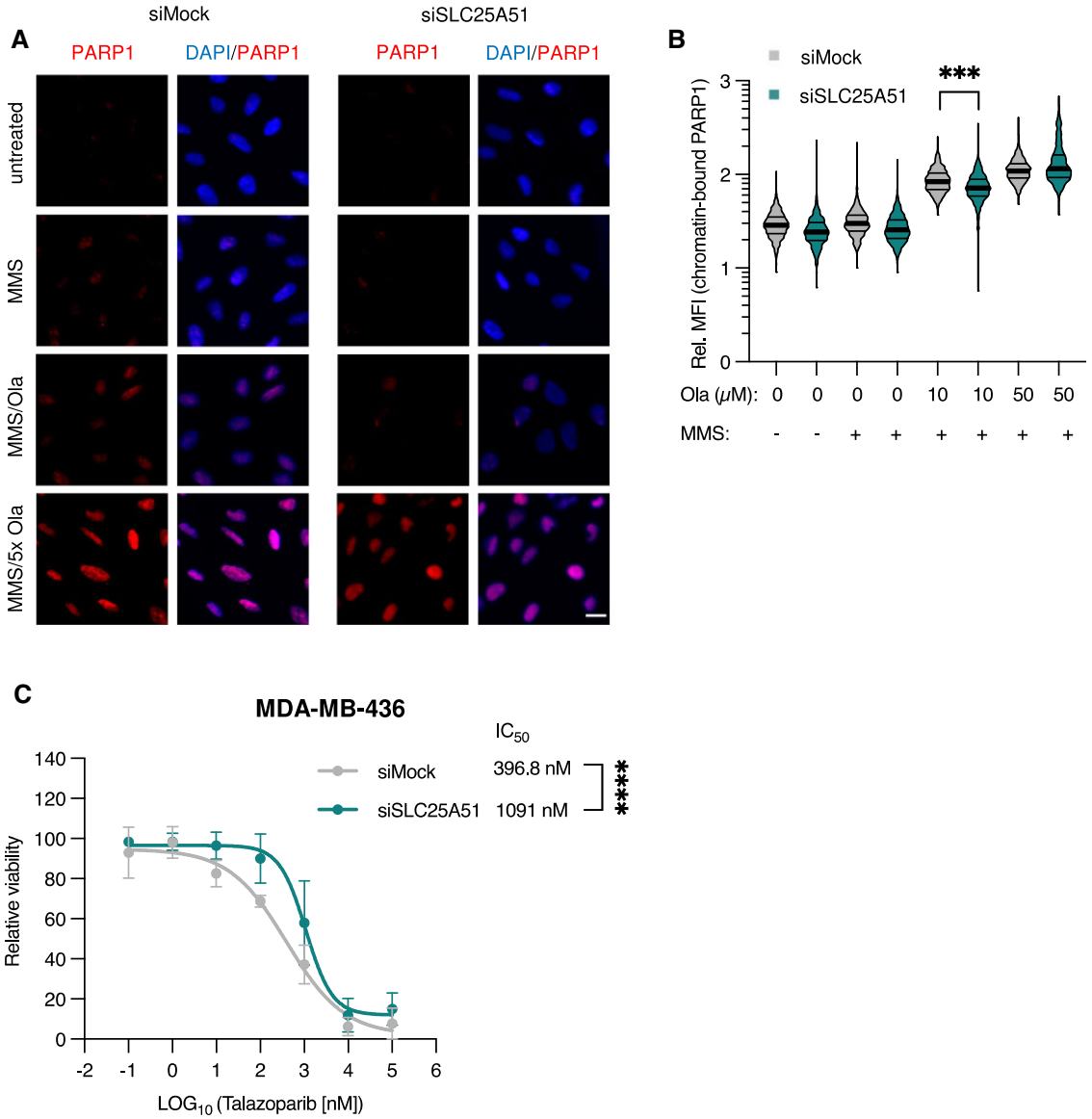

Figure 6. SLC25A51 knockdown decreases PARP1 chromatin retention and sensitivity to PARP inhibitors. (A and B) 48 h after knockdown of SLC25A51, U2OS cells were treated with 0.01% MMS and the indicated concentrations of Olaparib for 2 h and the chromatin retention of PARP1 was assessed by IF following pre-extraction (**A**) and quantified (**B**). One representative result of five independent experiments is shown. *P* values were determined by unpaired (for untreated cells) or paired (for treated cells), two-tailed Student's t-test comparing siSLC25A51 to siMock for each time point, using means from four independent experiments. (**C**) Following knockdown of SLC25A51 for 24 h, MDA-MB-436 cells were treated with Talazoparib for 6 days and cell viability was analyzed by resazurin assay. Relative cell numbers were normalized to DMSO-treated cells for siMock and siSLC25A51 respectively. *P* value was determined by comparing IC_{50}s calculated from two independent experiments by unpaired, two-tailed Student's *t*-test. *** $P < 0.0005$, **** $P < 0.00005$, ns (not significant) not shown; IF quantifications show one representative result of at least three independent experiments; scale bars indicate 20 μm.

precursors occurs in different cellular compartments (7). While it was previously reported that the NAD^+ precursor NMN can diffuse between the nucleus and cytoplasm (34), the shuttling of endogenous NAD^+ between the two compartments has never been shown before. NAD^+ diffusion through the nuclear pore complex has recently been shown by transfection of fluorescently-labeled NAD^+, however, the diffusion limit is known to change in response to different conditions, thus, a modified NAD^+ might not reflect the biological reality (13). However, our results support the notion that endogenous NAD^+ can freely diffuse between cytoplasm and nucleus. In case of high NAD^+ demands due to PARP1 hyperactivation, NMNAT1 binds to PAR and stimulates PARP1 activity (51). Further, NMNAT1 knockout alone was previously shown to inhibit PARP1 activity under conditions of genotoxic stress, resulting in increased γH2AX formation and reduced repair capacity (52). Thus, NMNAT1 is thought to directly resynthesize NAD^+ which is immediately utilized by PARP1. The direct interaction between NMNAT1 and PARP1 creates a microdomain which might separate nuclear and cytoplasmic NAD^+ under these conditions. Outside of an extreme activation like this, however, the cytoplasmic and nuclear NAD^+ pools are likely connected via the nuclear pore.

The finding that SLC25A51 knock-down could not restore the NAD^+ levels after NAMPT knock-down indicates that the increase in cytonuclear NAD^+ levels is indeed due to an accumulation of constitutively synthesized NAD^+ rather than a compensatory increase in salvage pathway activity. Furthermore, the decrease in mitochondrial NAD^+ levels in absence of SLC25A51 implies that most mitochondrial NAD^+ is synthesized in the nucleus and cytoplasm and subsequently taken up by the mitochondria via SLC25A51. Thus, we identified in cultured U2OS cells a flux of NAD^+ from the nucleo-cytoplasmic compartment to the mitochondria. While the contribution of NMNATs is undoubtedly important for the local synthesis of NAD^+ from NMN, already synthesized NAD^+ may well be able to move between compartments and be consumed without prior reconversion.

We could further demonstrate that absence of SLC25A51 and concomitantly decreased mitochondrial NAD^+ levels led to reduced mitochondrial ADP-ribosylation. These results are in line with a previous study where we showed that pharmacological manipulation of NAD^+ levels also dampens mitochondrial ADP-ribosylation (28). Together, both results suggest that mitochondrial ADP-ribosylation is at least partially dependent on nucleo-cytoplasmic NAD^+ availability and prove that ADP-ribosylation takes place within mitochondria even though the responsible mitochondrial writers are still not known. In contrast to mitochondrial ADP-ribosylation, nuclear ADP-ribosylation increased following knockdown or knockout of SLC25A51. Moreover, knockdown of SLC25A51 resulted in stronger nuclear ADP-ribosylation following either H_2O_2 or MMS treatment which likely results from delayed exhaustion of NAD^+ due to inhibited mitochondrial uptake of regenerated NAD^+ and storage. This is supported by NAD^+ measurements showing that in contrast to control cells, nuclear NAD^+ levels of SLC25A51 knockdown cells remained high after H_2O_2 treatment. Since H_2O_2 and MMS induce different types of DNA damage, this is likely to be a general effect of SLC25A51 on the SSB DNA damage response. Furthermore, cells lacking SLC25A51 repaired DNA damage faster not only under stress but also under baseline conditions, as evidenced by the reduced number of DNA lesions in resting cells. To our knowledge, such steady-state ADP-ribosylation and its involvement in the DNA damage repair in unstressed cells has not been shown before. In the context of single-strand damage, γH2AX is induced when SSBs induced by agents like H_2O_2 and MMS are incorporated as DSBs during replication (40,53). SLC25A51 depleted cells showed lower γH2AX signals following different DNA damage stimuli in a PARP1-dependent manner. Since DSBs are the most toxic type of DNA lesion, the faster SSB repair observed with SLC25A51 knockdown prevents the incorporation of DSBs during replication and provides a significant advantage.

The increase in nuclear ADP-ribosylation in cells lacking SLC25A51 depends on PARP1, which is not surprising given that PARP1 has the highest affinity for NAD^+ among the nuclear NAD^+ converting enzymes (54) and was shown here to be the most highly expressed ART in HAP1 and U2OS cells. Since PARP1 functions upstream of γH2AX in the DNA damage response, a full knockdown or knockout of PARP1 would directly affect γH2AX accumulation, leading to a decreased signal which is not indicative of better repair but of impaired signaling (55). We therefore used Olaparib to show that the observed improvement in SSB repair is dependent on ADP-ribosylation. Since Olaparib also inhibits other members of the ART family, especially PARP2, an involvement of PARP2 or another ART in the improved DNA damage response in cells lacking SLC25A51 cannot be excluded. However, only PARP1 is required for the increase in nuclear ADP-ribosylation and it is therefore likely that PARP1 is also responsible for the improved DNA damage response. NAD^+ is known to play a crucial role in the DNA damage response because it is utilized by the PARPs, especially PARP1, but also the Sirtuins and potentially certain DNA ligases (56). Reduced NAD^+ levels were shown to reduce XRCC1 recruitment, a PARP1 target, and leading to an accumulation of DNA damage and reduced repair capacity (57). Conversely, increased NAD^+ levels and increased PARP1 activity likely allow PARP1 to be evicted from chromatin by rapidly recruited XRCC1 and, thus, allow XRCC1 to induce the repair of the DNA lesion (58). In line with our findings, increasing NAD^+ levels by supplementing cells or mice with different types of NAD^+ precursors including nicotinamide and nicotinamide riboside also increased DNA repair efficiency in response to various DNA damage inducing agents both in healthy models and under conditions of neurodegeneration and aging, where NAD^+ levels are reduced (59,60).

While the higher nuclear NAD^+ levels in SLC25A51 deficient cells allow for a better DNA damage response, absence of SLC25A51 almost entirely abolishes OXPHOS and strongly reduces TCA intermediate levels (16–18) and therefore compromises cellular energy generation as well as synthesis of important small molecules, such as ATP or acetyl-CoA, resulting in a clear proliferation defect. It is intriguing to speculate that SLC25A51 might be involved in regulating NAD^+ distribution into different cellular compartments, effectively balancing the cell's need for NAD^+ for its different functions. However, how the transporter's expression and activity are regulated is not fully understood. Here, we show that the DNA damage response can be improved at the expense of mitochondrial function and proliferation. It is possible that different stressors that lead to higher NAD^+ requirements in specific compartments could regulate SLC25A51 in a similar way. Given that ADP-ribosylation in the nucleus was shown to be involved in various processes beyond the DNA damage response, e.g. gene expression, replication and the circadian rhythm (61), it would be interesting to determine if and how any of the involved pathways are affected by ADP-ribosylation in SLC25A51-deficient cells. Several metabolic enzymes have previously been shown to be regulated via ADP-ribosylation (e.g. hexokinase or GAPDH (3)), highlighting ADP-ribosylation as a candidate process that could contribute to the metabolic changes that occur in the absence of SLC25A51. Furthermore, once structurally important residues of SLC25A51 are determined, point mutations that specifically disrupt transporter function could be tested in regards to cytoplasmic and nuclear NAD^+ levels.

In addition to its direct effect on ADP-ribosylation, knockdown of SLC25A51 also decreased PARP1

chromatin retention following co-treatment with PARP inhibitors and DNA alkylating agents. As increased concentrations of PARP inhibitors were able to restore the chromatin retention of PARP1, the observed reduction was very likely a result of increased nuclear NAD^+ levels outcompeting the inhibitor and thus allowing for PARP1 to auto-modify itself. To highlight that nucleo-cytoplasmic NAD^+ levels might be relevant in PARPi therapy, we tested the PARPi sensitivity of triple negative MDA-MB-436 cells while modifying nuclear NAD^+ levels by knockdown of SLC25A51 and found reduced PARPi sensitivity in absence of SLC25A51. Some tumors overexpress SLC25A51 (62), which may imply that mitochondrial NAD^+ is more important for excessive proliferation compared to a faster DNA damage response. This makes SLC25A51 an intriguing target for pharmacological inhibition, which would likely result in decreased cancer cell proliferation. However, whether the improved DNA repair in absence of SLC25A51 is an advantage for cancer cells would have to be clarified *in vivo*. For cancer treatments based on PARP inhibitors, the additional inhibition of SLC25A51 would likely reduce their effect as shown here. Cancers that overexpress SLC25A51, on the other hand, may have lower nuclear NAD^+ levels because more NAD^+ is transported into the mitochondria, which could increase sensitivity to PARP inhibitors.

DATA AVAILABILITY

The raw data have been deposited to Mendeley data with the dataset identifier doi:10.17632/t899rgx3nv.1. All relevant mass spectrometry data have been deposited to the ProteomeXchange Consortium via the PRIDE (http://www.ebi.ac.uk/pride) partner repository with the data set identifier PXD031373.

SUPPLEMENTARY DATA

Supplementary Data are available at NAR Online.

ACKNOWLEDGEMENTS

We thank Patrick Grüther, and Tobias Suter (University of Zurich) as well as S. Andreas Angermayr (CeMM) for technical support and for providing editorial assistance, respectively. We further thank Enrico Girardi (Boehringer Ingelheim, formerly CeMM) for the generation of the stable HAP1 SLC25A51 knockout cell line. Inducible SLC25A51 overexpressing JumpIn HEK cells were generated by the RESOLUTE project 'https://re-solute.eu/'. We thank the Center for Microscopy and Image Analysis of the University of Zurich for services and assistance. The graphical abstract was created with biorender.com under the publication license HO25MOX6V9.

Author contributions: Project conceptualization and administration: A.-K.H. and M.O.H. (lead), A.G. (supporting), Data curation and Formal analysis: A-K.H. and A.G. (lead), L.M. and C.D. (supporting), Investigation (specific experiments): A.-K.H. and A.G. (lead), L.M., D.M.L.P. and P.M. (supporting), Visualization and validation: A.-K.H. and A.G., Methodology: A-K.H. and A.G. (lead), L.M. (supporting), Mass spec.: P.M. (lead) and A.G. (supporting), comet assays: C.D. (lead), biosensor: F.R., L.H. and K.J., Writing, review & editing of MS: M.O.H., A-K.H. and A.G. (lead), D.M.L.P. and G.S.F. (supporting).

FUNDING

Innovative Medicines Initiative 2 Joint Undertaking (JU) [777372 to G.S.F.], which receives support from the European Union's Horizon 2020 research and innovation program and EFPIA; Max Planck Society; Ecole Polytechnique Federale de Lausanne (EPFL); Deutsche Forschungsgemeinschaft (DFG, German Research Foundation) [TRR 186]; L.H. was supported by the Heidelberg Biosciences International Graduate School (HBIGS); University of Zurich (UZH) and Swiss National Science Foundation [31003A_176177 and 310030_205202 to M.O.H.]. Funding for open access charge: Swiss National Science Foundation.

Conflict of interest statement. None declared.

REFERENCES

1. Timmis,J.N., Ayliffe,M.A., Huang,C.Y. and Martin,W. (2004) Endosymbiotic gene transfer: organelle genomes forge eukaryotic chromosomes. *Nat. Rev. Genet.*, **5**, 123–135.
2. Pan,D., Lindau,C., Lagies,S., Wiedemann,N. and Kammerer,B. (2018) Metabolic profiling of isolated mitochondria and cytoplasm reveals compartment-specific metabolic responses. *Metabolomics*, **14**, 59.
3. Hopp,A.K., Grüter,P. and Hottiger,M.O. (2019) Regulation of glucose metabolism by NAD(+) and ADP-ribosylation. *Cells*, **8**, 890.
4. Hikosaka,K., Ikutani,M., Shito,M., Kazuma,K., Gulshan,M., Nagai,Y., Takatsu,K., Konno,K., Tobe,K., Kanno,H. *et al.* (2014) Deficiency of nicotinamide mononucleotide adenylyltransferase 3 (nmnat3) causes hemolytic anemia by altering the glycolytic flow in mature erythrocytes. *J. Biol. Chem.*, **289**, 14796–14811.
5. Jayaram,H.N., Kusumanchi,P. and Yalowitz,J.A. (2011) NMNAT expression and its relation to NAD metabolism. *Curr. Med. Chem.*, **18**, 1962–1972.
6. Berger,F., Lau,C., Dahlmann,M. and Ziegler,M. (2005) Subcellular compartmentation and differential catalytic properties of the three human nicotinamide mononucleotide adenylyltransferase isoforms. *J. Biol. Chem.*, **280**, 36334–36341.
7. Liu,L., Su,X., Quinn,W.J., Hui,S., Krukenberg,K., Frederick,D.W., Redpath,P., Zhan,L., Chellappa,K., White,E. *et al.* (2018) Quantitative analysis of NAD synthesis-breakdown fluxes. *Cell Metab.*, **27**, 1067–1080.
8. Svoboda,P., Krizova,E., Sestakova,S., Vapenkova,K., Knejzlik,Z., Rimpelova,S., Rayova,D., Volfova,N., Krizova,I., Rumlova,M. *et al.* (2019) Nuclear transport of nicotinamide phosphoribosyltransferase is cell cycle-dependent in mammalian cells, and its inhibition slows cell growth. *J. Biol. Chem.*, **294**, 8676–8689.
9. Fortunato,C., Mazzola,F. and Raffaelli,N. (2022) The key role of the NAD biosynthetic enzyme nicotinamide mononucleotide adenylyltransferase in regulating cell functions. *IUBMB Life*, **74**, 562–572.
10. Raices,M. and D'angelo,M.A. (2022) Structure, maintenance, and regulation of nuclear pore complexes: the gatekeepers of the eukaryotic genome. *Cold Spring Harb. Perspect. Biol.*, **14**, a040691.
11. Strambio-De-Castillia,C., Niepel,M. and Rout,M.P. (2010) The nuclear pore complex: bridging nuclear transport and gene regulation. *Nat. Rev. Mol. Cell Biol.*, **11**, 490–501.
12. Koch-Nolte,F., Fischer,S., Haag,F. and Ziegler,M. (2011) Compartmentation of NAD+-dependent signalling. *FEBS Lett.*, **585**, 1651–1656.
13. Lehner,M., Rieth,S., Höllmüller,E., Spliesgar,D., Mertes,B., Stengel,F. and Marx,A. (2022) Profiling of the ADP-ribosylome in living cells. *Angew. Chem. Int. Ed Engl.*, **61**, e202200977.

14. Ryu,K.W., Nandu,T., Kim,J., Challa,S., Deberardinis,R.J. and Kraus,W.L. (2018) Metabolic regulation of transcription through compartmentalized NAD(+) biosynthesis. *Science*, **360**, 6389.
15. Stein,L.R. and Imai,S.-I. (2012) The dynamic regulation of NAD metabolism in mitochondria. *Trends Endocrinol. Metab.*, **23**, 420–428.
16. Girardi,E., Agrimi,G., Goldmann,U., Fiume,G., Lindinger,S., Sedlyarov,V., Srndic,I., Gürtl,B., Agerer,B., Kartnig,F. *et al.* (2020) Epistasis-driven identification of SLC25A51 as a regulator of human mitochondrial NAD import. *Nat. Commun.*, **11**, 6145.
17. Kory,N., Uit De Bos,J., Van Der Rijt,S., Jankovic,N., Güra,M., Arp,N., Pena,I.A., Prakash,G., Chan,S.H., Kunchok,T. *et al.* (2020) MCART1/SLC25A51 is required for mitochondrial NAD transport. *Sci. Adv.*, **6**, 43.
18. Luongo,T.S., Eller,J.M., Lu,M.-J., Niere,M., Raith,F., Perry,C., Bornstein,M.R., Oliphint,P., Wang,L., Mcreynolds,M.R. *et al.* (2020) SLC25A51 is a mammalian mitochondrial NAD(+) transporter. *Nature*, **588**, 174–179.
19. Munnur,D. and Ahel,I. (2017) Reversible mono-ADP-ribosylation of DNA breaks. *FEBS J.*, **284**, 4002–4016.
20. Hottiger,M.O., Hassa,P.O., Lüscher,B., Schüler,H. and Koch-Nolte,F. (2010) Toward a unified nomenclature for mammalian ADP-ribosyltransferases. *Trends Biochem. Sci*, **35**, 208–219.
21. Weixler,L., Schäringer,K., Momoh,J., Lüscher,B., Feijs,K.L.H. and Žaja,R. (2021) ADP-ribosylation of RNA and DNA: from in vitro characterization to in vivo function. *Nucleic Acids Res.*, **49**, 3634–3650.
22. Cohen,M.S. (2020) Interplay between compartmentalized NAD(+) synthesis and consumption: a focus on the PARP family. *Genes Dev.*, **34**, 254–262.
23. Farmer,H., Mccabe,N., Lord,C.J., Tutt,A.N.J., Johnson,D.A., Richardson,T.B., Santarosa,M., Dillon,K.J., Hickson,I., Knights,C. *et al.* (2005) Targeting the DNA repair defect in BRCA mutant cells as a therapeutic strategy. *Nature*, **434**, 917–921.
24. Bryant,H.E., Schultz,N., Thomas,H.D., Parker,K.M., Flower,D., Lopez,E., Kyle,S., Meuth,M., Curtin,N.J. and Helleday,T. (2005) Specific killing of BRCA2-deficient tumours with inhibitors of poly(ADP-ribose) polymerase. *Nature*, **434**, 913–917.
25. Lord,C.J. and Ashworth,A.: (2017) Synthetic lethality in the clinic. *Science*, **355**, 1152–1158.
26. Ashworth,A., Lord,C.J. and Reis-Filho,J.S. (2011) Genetic interactions in cancer progression and treatment. *Cell*, **145**, 30–38.
27. Azarm,K. and Smith,S. (2020) Nuclear parps and genome integrity. *Genes Dev.*, **34**, 285–301.
28. Hopp,A.-K., Teloni,F., Bisceglie,L., Gondrand,C., Raith,F., Nowak,K., Muskalla,L., Howald,A., Pedrioli,P.G.A., Johnsson,K. *et al.* (2021) Mitochondrial NAD(+) controls nuclear ARTD1-induced ADP-ribosylation. *Mol. Cell*, **81**, 340–354.
29. Hendriks,I.A., Larsen,S.C. and Nielsen,M.L. (2019) An advanced strategy for comprehensive profiling of ADP-ribosylation sites using mass spectrometry-based proteomics. *Mol. Cell. Proteomics*, **18**, 1010–1026.
30. Szczesny,B., Brunyanszki,A., Olah,G., Mitra,S. and Szabo,C. (2014) Opposing roles of mitochondrial and nuclear PARP1 in the regulation of mitochondrial and nuclear DNA integrity: implications for the regulation of mitochondrial function. *Nucleic Acids Res.*, **42**, 13161–13173.
31. Módis,K., Gerő,D., Erdélyi,K., Szoleczky,P., Dewitt,D. and Szabo,C. (2012) Cellular bioenergetics is regulated by PARP1 under resting conditions and during oxidative stress. *Biochem. Pharmacol.*, **83**, 633–643.
32. Sallin,O., Reymond,L., Gondrand,C., Raith,F., Koch,B. and Johnsson,K. (2018) Semisynthetic biosensors for mapping cellular concentrations of nicotinamide adenine dinucleotides. *eLife*, **7**, e32638.
33. Davila,A., Liu,L., Chellappa,K., Redpath,P., Nakamaru-Ogiso,E., Paolella,L.M., Zhang,Z., Migaud,M.E., Rabinowitz,J.D. and Baur,J.A. (2018) Nicotinamide adenine dinucleotide is transported into mammalian mitochondria. *eLife*, **7**, e33246.
34. Luo,X., Ryu,K.W., Kim,D.-S., Nandu,T., Medina,C.J., Gupte,R., Gibson,B.A., Soccio,R.E., Yu,Y., Gupta,R.K. *et al.* (2017) PARP-1 controls the adipogenic transcriptional program by parylating C/EBPbeta and modulating its transcriptional activity. *Mol. Cell*, **65**, 260–271.
35. Michelena,J. and Altmeyer,M. (2017) Cell cycle resolved measurements of poly(ADP-Ribose) formation and DNA damage signaling by quantitative image-based cytometry. *Methods Mol. Biol.*, **1608**, 57–68.
36. Toledo,L.I., Altmeyer,M., Rask,M.-B., Lukas,C., Larsen,D.H., Povlsen,L.K., Bekker-Jensen,S., Mailand,N., Bartek,J. and Lukas,J. (2013) ATR prohibits replication catastrophe by preventing global exhaustion of RPA. *Cell*, **155**, 1088–1103.
37. Nowak,K., Rosenthal,F., Karlberg,T., Bütepage,M., Thorsell,A.-G., Dreier,B., Grossmann,J., Sobek,J., Imhof,R., Lüscher,B. *et al.* (2020) Engineering Af1521 improves ADP-ribose binding and identification of ADP-ribosylated proteins. *Nat. Commun.*, **11**, 5199.
38. Bilan,V., Leutert,M., Nanni,P., Panse,C. and Hottiger,M.O. (2017) Combining HCD and EThcD fragmentation in a product dependent-manner confidently assigns proteome-wide ADP-ribose acceptor sites. *Anal. Chem.*, **89**, 1523–1530.
39. Martello,R., Leutert,M., Jungmichel,S., Bilan,V., Larsen,S.C., Young,C., Hottiger,M.O. and Nielsen,M.L. (2016) Proteome-wide identification of the endogenous ADP-ribosylome of mammalian cells and tissue. *Nat. Commun.*, **7**, 12917.
40. Ray Chaudhuri,A. and Nussenzweig,A. (2017) The multifaceted roles of PARP1 in DNA repair and chromatin remodelling. *Nat. Rev. Mol. Cell Biol.*, **18**, 610–621.
41. Stiff,T., O'driscoll,M., Rief,N., Iwabuchi,K., LöBrich,M. and Jeggo,P.A. (2004) ATM and DNA-PK function redundantly to phosphorylate H2AX after exposure to ionizing radiation. *Cancer Res.*, **64**, 2390–2396.
42. Celeste,A., Difilippantonio,S., Difilippantonio,M.J., Fernandez-Capetillo,O., Pilch,D.R., Sedelnikova,O.A., Eckhaus,M., Ried,T., Bonner,W.M. and Nussenzweig,A. (2003) H2AX haploinsufficiency modifies genomic stability and tumor susceptibility. *Cell*, **114**, 371–383.
43. Liu,C., Vyas,A., Kassab,M.A., Singh,A.K. and Yu,X. (2017) The role of poly ADP-ribosylation in the first wave of DNA damage response. *Nucleic Acids Res.*, **45**, 8129–8141.
44. Polo,S.E. and Jackson,S.P. (2011) Dynamics of DNA damage response proteins at DNA breaks: a focus on protein modifications. *Genes Dev.*, **25**, 409–433.
45. Michelena,J., Lezaja,A., Teloni,F., Schmid,T., Imhof,R. and Altmeyer,M. (2018) Analysis of PARP inhibitor toxicity by multidimensional fluorescence microscopy reveals mechanisms of sensitivity and resistance. *Nat. Commun.*, **9**, 2678.
46. Hopkins,T.A., Ainsworth,W.B., Ellis,P.A., Donawho,C.K., Digiammarino,E.L., Panchal,S.C., Abraham,V.C., Algire,M.A., Shi,Y., Olson,A.M. *et al.* (2019) PARP1 Trapping by PARP inhibitors drives cytotoxicity in both cancer cells and healthy bone marrow. *Mol. Cancer Res.*, **17**, 409–419.
47. Litton,J.K., Rugo,H.S., Ettl,J., Hurvitz,S.A., Gonçalves,A., Lee,K.-H., Fehrenbacher,L., Yerushalmi,R., Mina,L.A., Martin,M. *et al.* (2018) Talazoparib in patients with advanced breast cancer and a germline BRCA mutation. *N. Engl. J. Med.*, **379**, 753–763.
48. Robson,M., Im,S.-A., Senkus,E.ż, Xu,B., Domchek,S.M., Masuda,N., Delaloge,S., Li,W., Tung,N., Armstrong,A. *et al.* (2017) Olaparib for metastatic breast cancer in patients with a germline BRCA mutation. *N. Engl. J. Med.*, **377**, 523–533.
49. Keung,M., Wu,Y. and Vadgama,J. (2019) PARP inhibitors as a therapeutic agent for homologous recombination deficiency in breast cancers. *J. Clin. Med.*, **8**, 435.
50. Keung,M.Y., Wu,Y., Badar,F. and Vadgama,J.V. (2020) Response of breast cancer cells to PARP inhibitors is independent of BRCA status. *J. Clin. Med.*, **9**, 940.
51. Berger,F., Lau,C. and Ziegler,M. (2007) Regulation of poly(ADP-ribose) polymerase 1 activity by the phosphorylation state of the nuclear NAD biosynthetic enzyme NMN adenylyl transferase 1. *Proc. Natl. Acad. Sci. U.S.A.*, **104**, 3765–3770.
52. Kiss,A., Ráduly,A.P., Regdon,Z., Polgár,Z., Tarapcsák,S., Sturniolo,I., El-Hamoly,T., Virág,L. and Hegedűs,C. (2020) Targeting nuclear NAD(+) synthesis inhibits DNA repair, impairs metabolic adaptation and increases chemosensitivity of U-2OS osteosarcoma cells. *Cancers (Basel)*, **12**, 1180.
53. Chatterjee,N. and Walker,G.C. (2017) Mechanisms of DNA damage, repair, and mutagenesis. *Environ. Mol. Mutagen.*, **58**, 235–263.

54. Cantó,C., Sauve,A.A. and Bai,P. (2013) Crosstalk between poly(ADP-ribose) polymerase and sirtuin enzymes. *Mol. Aspects Med.*, **34**, 1168–1201.
55. Aguilar-Quesada,R., Muñoz-Gámez,J.A., Martín-Oliva,D., Peralta,A., Valenzuela,M.T., Matínez-Romero,R., Quiles-Pérez,R., Murcia,J.M.-D., De Murcia,G., De Almodóvar,M.R. *et al.* (2007) Interaction between ATM and PARP-1 in response to DNA damage and sensitization of ATM deficient cells through PARP inhibition. *BMC Mol. Biol.*, **8**, 29.
56. Ruszkiewicz,J.A., Bürkle,A. and Mangerich,A. (2022) Fueling genome maintenance: on the versatile roles of NAD(+) in preserving DNA integrity. *J. Biol. Chem.*, **298**, 102037.
57. Wilk,A., Hayat,F., Cunningham,R., Li,J., Garavaglia,S., Zamani,L., Ferraris,D.M., Sykora,P., Andrews,J., Clark,J. *et al.* (2020) Extracellular NAD(+) enhances PARP-dependent DNA repair capacity independently of CD73 activity. *Sci. Rep.*, **10**, 651.
58. Demin,A.A., Hirota,K., Tsuda,M., Adamowicz,M., Hailstone,R., Brazina,J., Gittens,W., Kalasova,I., Shao,Z., Zha,S. *et al.* (2021) XRCC1 prevents toxic PARP1 trapping during DNA base excision repair. *Mol. Cell*, **81**, 3018–3030.
59. Weidele,K., Beneke,S. and Bürkle,A. (2017) The NAD(+) precursor nicotinic acid improves genomic integrity in human peripheral blood mononuclear cells after X-irradiation. *DNA Repair (Amst.)*, **52**, 12–23.
60. Fang,E.F., Kassahun,H., Croteau,D.L., Scheibye-Knudsen,M., Marosi,K., Lu,H., Shamanna,R.A., Kalyanasundaram,S., Bollineni,R.C., Wilson,M.A. *et al.* (2016) NAD(+) replenishment improves lifespan and healthspan in Ataxia Telangiectasia models via mitophagy and DNA repair. *Cell Metab.*, **24**, 566–581.
61. Hottiger,M.O. (2015) Nuclear ADP-ribosylation and its role in chromatin plasticity, cell differentiation, and epigenetics. *Annu. Rev. Biochem.*, **84**, 227–263.
62. Regev,A., Teichmann,S.A., Lander,E.S., Amit,I., Benoist,C., Birney,E., Bodenmiller,B., Campbell,P., Carninci,P., Clatworthy,M. *et al.* (2017) The Human cell atlas. *eLife*, **6**, e27041.
63. Minotti,R., Andersson,A. and Hottiger,M.O. (2015) ARTD1 Suppresses interleukin 6 expression by repressing MLL1-dependent histone H3 trimethylation. *Mol. Cell. Biol.*, **35**, 3189–3199.
64. Ostasiewicz,P., Zielinska,D.F., Mann,M. and Wiśniewski,J.R. (2010) Proteome, phosphoproteome, and N-glycoproteome are quantitatively preserved in formalin-fixed paraffin-embedded tissue and analyzable by high-resolution mass spectrometry. *J. Proteome Res.*, **9**, 3688–3700.
65. Leutert,M., Menzel,S., Braren,R., Rissiek,B., Hopp,A.-K., Nowak,K., Bisceglie,L., Gehrig,P., Li,H., Zolkiewska,A. *et al.* (2018) Proteomic characterization of the heart and skeletal muscle reveals widespread arginine ADP-ribosylation by the ARTC1 ectoenzyme. *Cell Rep.*, **24**, 1916–1929.
66. Gehrig,P.M., Nowak,K., Panse,C., Leutert,M., Grossmann,J., Schlapbach,R. and Hottiger,M.O. (2021) Gas-phase fragmentation of ADP-ribosylated peptides: arginine-specific side-chain losses and their implication in database searches. *J. Am. Soc. Mass. Spectrom.*, **32**, 157–168.